Rheology and mechanical properties of limestone calcined clay based engineered cementitious composites with nano $CaCO_3$

Yuting Wang [a], Meng Chen [a,b,*], Tong Zhang [a], Mingzhong Zhang [c]

[a] *School of Resources and Civil Engineering, Northeastern University, Shenyang, 110819, China*

[b] *Institute for Frontier Technologies of Low-Carbon Steelmaking, Northeastern University, Shenyang, 110819, China*

[c] *Department of Civil, Environmental and Geomatic Engineering, University College London, London, WC1E 6BT, UK*

Abstract: The application of binder consisting of limestone, calcined clay and cement (LC^3) promotes the development of low-carbon engineering cementitious composites (ECC). In order to improve the comprehensive properties of LC^3-ECC, this paper investigates the feasibility of using nano $CaCO_3$ (NC) to replace the limestone powder up to 20% for LC^3-ECC preparation through rheology and mechanical tests along with the micro-design calculation and microstructure analysis. Results indicate that the yield stress and plastic viscosity of LC^3-ECC are largely improved with increasing NC replacement rate. Meanwhile, the compressive, flexural and tensile strengths of LC^3-ECC with NC raise firstly and then decline, while the strengths are maximum at NC replacement rate of 5% but the tensile strain capacity remains at 2.3%. The hydration promotion effect and pore structure refinement effect of NC particles improve the mechanical strength of LC^3-ECC, but the performance degradation occurs when the replacement rate of the NC exceeds 10%. In micromechanics, the fibre bridging stress of LC^3-ECC reinforced by NC with replacement rate of 5% decreases by 18.5% compared to that of without NC, but it grows with the increasing NC replacement rate. In combination with fresh, hardened and microstructure behaviour, LC^3-ECC exhibits the optimum mechanical behaviour with the NC replacement rate of 10%–15%.

Keywords: Engineered Cementitious Composites; Limestone calcined clay cement; Nano $CaCO_3$; Rheology; Strain hardening behaviour; Micromechanics

* Corresponding author.

E-mail addresses: chenmeng@mail.neu.edu.cn (M. Chen).

1. Introduction

Engineered cementitious composites (ECC), also known as strain hardening cementitious composites, is a type of ultra-high toughness materials with excellent deformability and energy absorption [1,2]. Since its development in the 1990s, ECC has achieved exceptional performance in strain hardening behaviour and multiple cracking capacity [3]. Based on the effective bridging effect provided by reinforced fibre such as polyvinyl alcohol (PVA) fibre and polyethylene (PE) fibre, ECC exhibits tensile strain of over 2% and cracking width of less than 100 μm [4,5]. However, due to the more than 50 wt% of binder in ECC, supplementary cementitious materials have been used to replace partial cement for a more environmentally friendly ECC development [6–8]. Among them, limestone calcined clay cement (LC^3) has been focused and investigated to have comparable mechanical strength with ordinary cement paste [9,10]. Furthermore, ECC produced with LC^3 will have lower energy consumption and carbon emissions while achieving the similar high ductility of typical ECC [11,12].

The application of LC^3 has various effects on the both fresh and hardened properties of ECC. Owing to the high water absorption and specific surface area of LC^3, the flowability of ECC based on LC^3 with a mass ratio of 0.15:0.30:0.55 for limestone powder, calcined clay and cement is reduced by 34.6% than that of ordinary Portland cement (OPC) based ECC [13]. Moreover, the yield stress and plastic viscosity of LC^3-ECC in the rheological test are also raised by 0.67–1.85 and 0.08–0.85 times than that of ordinary ECC, respectively [14]. Hence, LC^3 based materials have also been successively utilised as a raw material for 3D printing cementitious materials that have exhibited favourable constructability and printability [15,16]. In terms of hardening properties, the incorporation of LC^3 improves the early-age mechanical properties of cementitious materials due to the nucleation sites of low reacted limestone powder [17,18]. With increasing percentage of LC^3 in the binders, the compressive strength is decreased due to the free moisture shortage and lower water-to-binder ratio of ECC [19–21]. Meanwhile, the tensile strength of ECC also decreases but the tensile strain capacity shows an improved performance with increasing LC^3 content, in which the tensile strain increased by 13.5 times when the strength decreased by 20.8% than OPC-ECC [22]. Besides, LC^3 is able to increase the fibre-to-matrix bond strength and fibre pull out energy, which makes it advantageous in the application of high-performance cementitious materials [19].

Nowadays, nanomaterials have been utilised to enhance the microstructure and the chemical reaction of cementitious materials in order to improve their mechanical performance. As an ultrafine materials with nano-sized particles of below 100 nm [23,24], nanomaterials mainly include nano SiO_2 [25,26], nano $CaCO_3$ [27] and nano TiO_2 [28], etc. In comparison, nano $CaCO_3$ (NC) is the most widespread, cheapest and widely available nano materials [29,30]. NC can enhance nucleation sites for cement particles and promote the formation of calcium-silicate-hydrate in order to shorten the cement hydration process [31]. In parallel, it improves the alignment position of calcium hydroxide and optimises the interfacial transition zone within the matrix [24]. Furthermore, NC can react with C3A within cement to improve the early strength of cementitious materials [32,33]. The microaggregate effect exhibited by NC optimises the pore size distribution of cementitious materials that improves their strength and durability [29,34]. Therefore, some researchers have been exploring the use of NC to improve the strength properties of ECC. Ding et al. [29] prepared ultra-high performance ECC using NC with more than 8% tensile strain at compressive strengths over 130 MPa, and suggested that the optimum content of NC is 3% by weight of the cement. Khokhar et al. [35] produced ECC directly using 1%–4% NC mixed with calcined clay and cement, where the compressive strength of the mortar increased with increasing NC content and the relationship between the NC content and the mechanical strength of ECC was not shown. Hence, the effect of NC on the macro performance of ECC needs to be systematically investigated through a comprehensive experiment. Considering the similarity between the composition of NC and limestone powder, the design of the proportion of NC is essential for the fresh/hardening properties when using NC to reinforce LC^3-ECC, as well as the effect on the microstructure evolution needs to be further explored.

This study focused on the fresh and mechanical behaviour of LC^3-ECC in which limestone powder was replaced by NC with ratio of 0, 5%, 10%, 15% and 20 % for each mixture. Firstly, rheological property tests were carried out to determine the flow characteristics of all mixtures. Then, mechanical tests including compressive, flexural and tensile tests were carried out to investigate the effect of NC incorporation on the strength and cracking behaviour of LC^3-ECC. Besides, the matrix properties and single-crack tensile behaviour of the LC^3-ECC reinforced with NC were determined in order to calculate the micromechanical parameters and assess whether it meets the design criteria. Finally, the phase composition, fibre morphology and microstructure were tested by X-ray

diffractometer (XRD), thermal analysis, scanning electron microscope-backscattered electron (SEM-BSE) and mercury intrusion porosimetry (MIP) to analyse the variation of macro properties from the micro perspective.

2. Experimental program

2.1. Raw materials

In this study, the P.I. 42.5 Portland cement, limestone powder and calcined clay were used to compose the LC^3 binder. According to ASTM C618 [36], the fly ash classified as Class F was used as supplementary cementitious materials. The oxide composition and particle size distribution are demonstrated at Table 1 and Fig. 1, respectively. The silica sand with particle size of 100–300 μm was used as fine aggregate. Polycarboxylate-based superplasticisers (SP) and viscosity modifying admixture (VMA) were used to adjust the workability of fresh mixtures. The oil-treated PVA fibre was used as reinforced fibre to ensure the toughness and deformability of cementitious composites. Relevant basic properties of PVA fibre are depicted in Table 2. The NC with particle size of 15–40 nm was used for replacing the limestone powder particles acting as fillers in the matrix and enhancing the matrix properties, which original morphology and XRD pattern are displayed in Fig. 2.

Table 1 Chemical proportions of raw materials (wt%).

Type/oxide	CaO	SiO_2	Al_2O_3	Fe_2O_3	SO_3	MgO	K_2O	TiO_2	ZrO_2
Cement	62.67	22.97	5.55	2.90	2.05	1.98	1.12	0.35	0.02
Limestone powder	95.65	0.08	0.10	0.10	–	0.34	0.01	–	0.01
Calcined clay	0.32	49.94	47.57	0.69	–	0.04	0.31	1.03	0.03
Fly ash	3.23	51.34	36.87	0.59	0.26	0.55	1.93	1.90	0.02

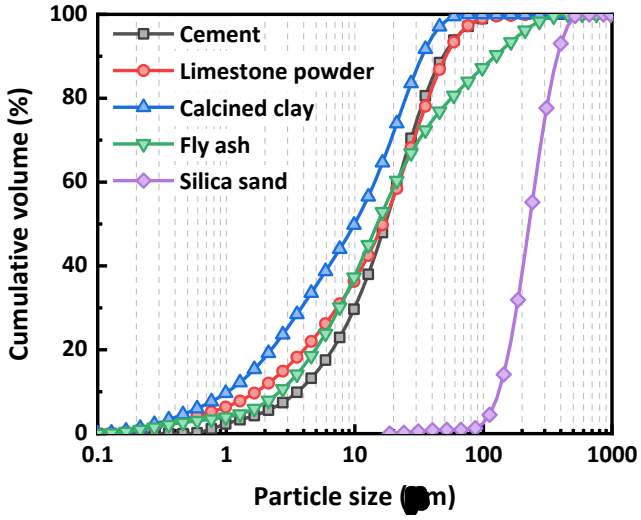

Fig. 1. Particle size distribution of the ingredients.

Table 2 Physical and mechanical properties of PVA fibres.

Diameter (μm)	Length (mm)	Density (kg/m^3)	Elastic modulus (GPa)	Tensile strength (MPa)
39	12	1280	40	≥1600

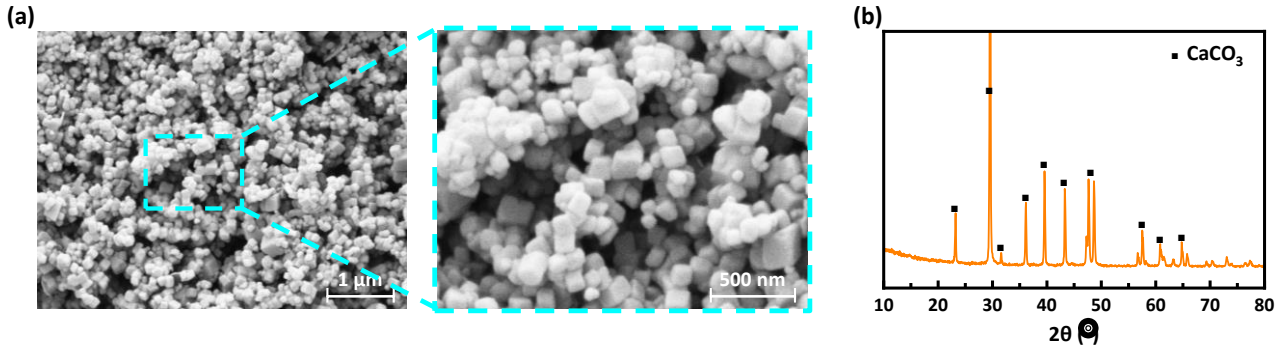

Fig. 2. Morphology and XRD pattern of NC granules.

2.2. Mix proportions

The typical LC^3 binder system consisting of 55% cement, 30% calcined clay and 15% limestone powder was regarded as the main reaction ingredients [21,37]. Using it as a reference, NC was used to replace the limestone powder in the percentages of 0%, 5%, 10%, 15% and 20%. Meanwhile, the fly ash of 1.2 times weight of the LC^3 was used in accordance with the M45-ECC mix proportion. The weight of silica sand accounted for 0.8 times of the LC^3 binder. The ratio of water to binder was set at 0.25. The content of SP and VMA were maintained at 0.55% and 0.15% by the total weight of LC^3 and fly ash. The PVA fibre content was set as 2 vol% of the total composites. The mix proportions of all mixtures in this study are listed in Table 3. In the example of 'N5', the intended meaning is that NC will serve as a substitute for the 5% limestone powder content present in the reference group of 'N0'.

Table 3 Mixture proportions of LC^3-ECC with NC (kg/m^3).

Mixture type	Cement	Calcined clay	Fly ash	Silica sand	Water	SP	VMA	PVA fibre	Limestone powder	NC
N0	299.2	163.2	652.8	435.2	299.2	6.5	1.8	26.0	81.6	0
N5	299.2	163.2	652.8	435.2	299.2	6.5	1.8	26.0	77.52	4.08
N10	299.2	163.2	652.8	435.2	299.2	6.5	1.8	26.0	73.44	8.16
N15	299.2	163.2	652.8	435.2	299.2	6.5	1.8	26.0	69.36	12.24
N20	299.2	163.2	652.8	435.2	299.2	6.5	1.8	26.0	65.28	16.32

2.3. Sample preparation

Owing to the particle size of NC is nano scale, the NC granules agglomeration is easy to occur

when it is directly added to the ECC mixing process. Therefore, it is necessary to conduct the disperse treatment for NC prior to the formal mixing progress. Firstly, the NC with fixed proportion was added to the corresponding weighed mixture of water and SP, followed by ultrasonic dispersion treatment for 10 min. Then, the mixing process of LC^3-ECC with total time of 13 min was carried out, as illustrated in Fig. 3. Finally, one part of fresh mixture was used for rheology test after the mixing process. Another part of mixture was moulded for tested specimen of different sizes and cured for 28 d (1 d for moulding and 27 d for standard curing) until the subsequent mechanical and microscopic test stage (see Fig. 3).

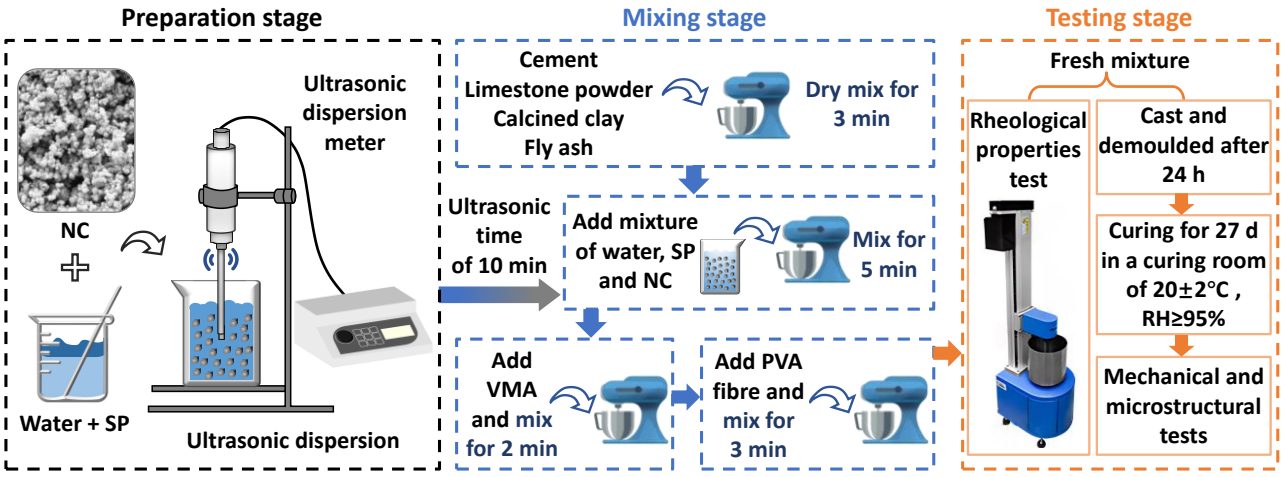

Fig. 3. Sample preparation process of NC reinforced LC^3-ECC.

2.4. Test methods

2.4.1. Rheology test

In the case of cementitious materials, the rheological properties mainly include static yield stress (τ_s), dynamic yield stress (τ_d) and plastic viscosity (η) to determine the flowability of fresh mixtures [38]. To measure the rheological properties of fresh NC reinforced LC^3-ECC, a rotational rheometer with cross-shaped blade was employed to achieve the effect of an internal cylindrical shaped rotation. After the mixing process, the fresh mixtures were poured to the rheometer vessel with 3.6 L capacity and prepared for formal test. Static yield stress was measured by shear stress increasing test, which lasted for 60 s at a fixed shear rate of 0.025 rps (corresponding to the shear rate of 0.225 /s) [39]. The static yield stress was calculated from the measured maximum torque (T_{max}) using the following equation:

$$\tau_s = \frac{2T_{max}}{\pi D^3 \left(\frac{H}{D} + \frac{1}{3}\right)} \quad (1)$$

where D and H are the diameter and height of the rotating vane, respectively.

Different shear programmes (including shear rate ranges, duration of each shear step, temperature, etc.) can lead to different responses or parametric results, thus a consistent programme should be maintained when testing different mixtures [40]. After a 40 s of pre-shear stage at a shear rate of 0.6 rps, dynamic yield stress and plastic viscosity of fresh mixtures were tested. The shear stress (τ) decreased from 0.6 rps to 0.05 rps (corresponding to the shear rate from 5.392 to 0.450 /s) after 24 steps with a residence time of 5 s for each step, as shown in Fig. 4. Then, the corresponding torque (T) and rotational velocity (N) were measured, as well as the T and N were converted into τ and shear rate ($\dot{\gamma}$) using Eq. (2) and Eq. (3), respectively [41,42]. The static and dynamic rheological property tests of all mixtures were repeated three times in the same environment to avoid the erroneous effects caused by temperature and humidity variations.

$$\tau = \frac{R_0^2 + R_i^2}{4\pi H R_0^2 R_i^2} T \quad (2)$$

$$\dot{\gamma} = \frac{R_0^2 + R_i^2}{R_0^2 - R_i^2} 2\pi N \quad (3)$$

where R_0 is the inner radius of the rheometer vessel, and R_i is the width of the rotating vane.

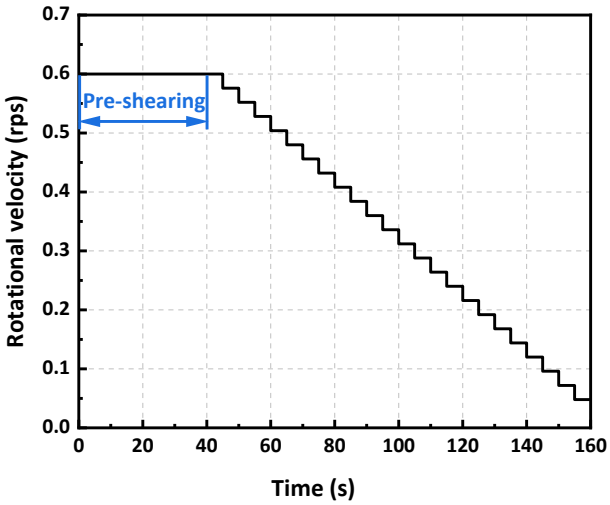

Fig. 4. Rheology test protocol.

2.4.2. Mechanical tests

The mechanical properties of NC-reinforced LC^3-ECC will be evaluated by developing

compressive, flexural, and uniaxial tensile tests. Meanwhile, the fracture toughness test of mortar matrix and single-crack tensile test of ECC were also performed to calculate the micromechanics design index of all mixtures. The compressive test was conducted on the 50 mm cubes with the loading rate of 0.3 MPa/s following ASTM C109/C109M-20b [43]. For the flexural test, prism specimens with size of 160 (l)×40 (b)×40 (h) mm^3 were subjected to three-point flexion at a rate of 2.0 mm/min according to GB/T 50081–2019 [44]. Uniaxial tensile tests were carried out on the dog-bone shaped specimens as per JSCE with loading rate of 0.5 mm/min [45]. Two linear variable displacement transducers (LVDTs) were arranged on both sides of the test specimen in order to gauge the strain within its tensile region of 80 mm length, as shown in Fig. 5.

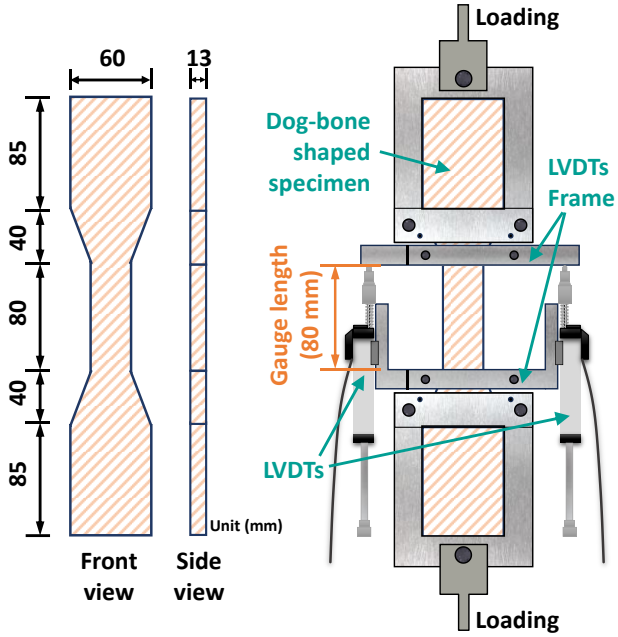

Fig. 5. Specimen dimension and experimental installation schematic of uniaxial tensile test.

Based on the micromechanical theory, ECC is designed to be provided with strain hardening and multiple cracking features [3]. The strength and energy criteria are the two quantitative conditions for determining whether a cementitious material satisfies the ECC design standards. Moreover, the two criteria can be interpreted based on typical tensile stress versus crack opening curves, as plotted in Fig. 6. The strength criterion (see Eq. (4)) means that the tensile strength of matrix (σ_{fc}) and the tensile stress to form the first or new crack (σ_c) need to be less than the fibre bridging stress (σ_0) [6]. In turn, the energy criterion (see Eq. (5)) refers to the fact that the tensile residual energy (J'_b) maximum needs to be greater than the crack tip toughness (J_{tip}), defined as the physical meaning of

the two different shaded areas in Fig. 6.

$$\sigma_0 > \sigma_{fc}, \sigma_c \tag{4}$$

$$J'_b \geq J_{tip} = \sigma_{ss}\delta_{ss} - \int_0^{\delta_{ss}} \sigma(\delta)\, d\delta \approx \frac{K_m^2}{E_m} \tag{5}$$

$$\sigma_0\delta_0 - \int_0^{\delta_0} \sigma(\delta)\, d\delta = J'_b \tag{6}$$

where δ_0 is the crack opening corresponding to the σ_0, δ_{ss} is the crack opening corresponding to the steadystate bridging stress (σ_{ss}), E_m and K_m are the elastic modulus and fracture toughness of the matrix, respectively.

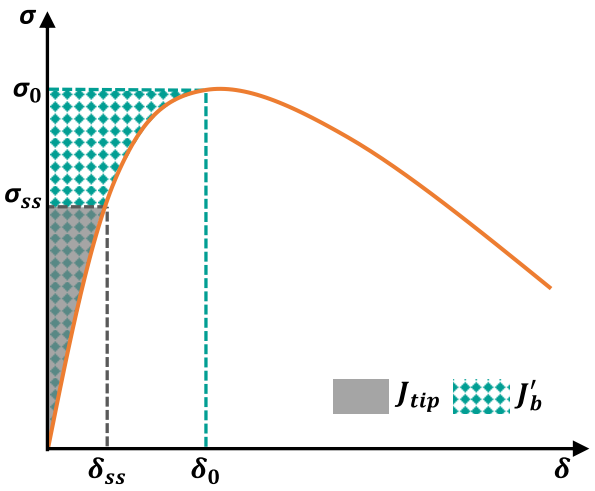

Fig. 6. Typical stress-crack opening curve for fibre bridging (adapted from Ref. [3]).

Based on the both design criteria, pseudo strain-hardening (PSH) indexes can be calculated, i.e. σ_0/σ_{fc} and J'_b/J_{tip}. The calculated values are used to determine the tensile characteristics of the mixtures. Therefore, the single crack tensile test of ECC was carried out to obtain the tensile stress-crack opening width curve and fibre bridging strength. Fig. 7a displays the single crack tensile test specimen and tested device. The loading rate was 0.5 mm/min and the amount of displacement change was measured by LVDTs. The tensile strength and elastic modulus of the matrix were obtained by conducting tensile tests on the mortar and calculating the slope of stress linearly increasing section of the curve. For the matrix fracture toughness test, a 12 mm deep crack was prefabricated at the bottom of the prismatic flexural specimen and three-point flexural loading with a loading rate of 1.0 mm/min was performed (Fig. 7b) as per RILEM FMC-50 [46]. The fracture toughness (K_m) can be calculated according to the following equation by Ref. [47]:

200 $$K_m = \frac{1.5\left(P_{max} + \frac{mg}{2} \times 10^{-2}\right) \times 10^{-\frac{3}{2}} \times S \times a_0^{\frac{1}{2}}}{bh^2} \times f(\alpha) \quad (7)$$

201 $$f(\alpha) = \frac{1.99 - \alpha(1-\alpha)(2.15 - 3.99\alpha + 2.7\alpha^2)}{(1+2\alpha)(1-\alpha)^{\frac{3}{2}}} \quad (8)$$

202 $$\alpha = \frac{a_0}{h} \quad (9)$$

203 where P_{max} is the load maximum of the fracture toughness test (N), m is the mass of tested specimen
204 (kg), S is the span length of the specimen (mm), a_0 is the notch depth, b and h are the width (mm)
205 and height (mm) of the tested specimen, respectively.

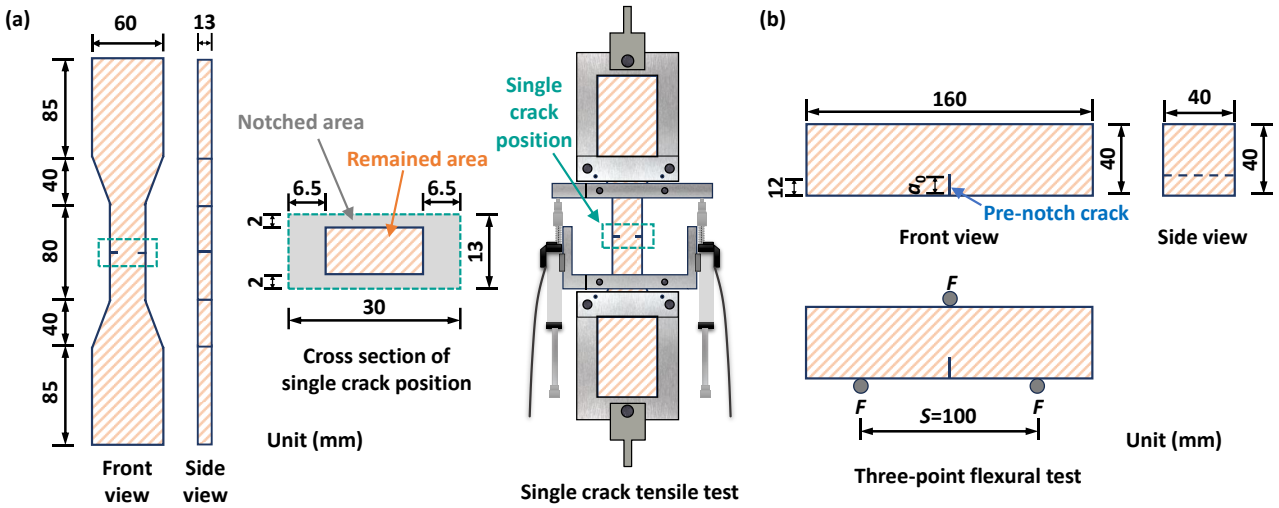

206

207 **Fig. 7.** Micromechanical test: (a) single crack tensile specimen and test setup; (b) three-point
208 flexural test for determining fracture toughness.

209 *2.4.3. X-ray diffraction test*

210 To clearly visualise the effect of NC on the physical phase composition, LC^3-ECC pastes in the
211 same mix proportions of mortar were prepared and measured by X-ray diffractometer (Rigaku, Smart
212 Lab SE). Powder samples with particle size lower than 75 μm obtained from the compressive tested
213 specimens were scanned from 5° to 65° with a scanning rate of 5°/min in the XRD test.

214 *2.4.4. Thermal analysis*

215 The powder samples of NC reinforced LC^3-ECC with particle size lower than 75 μm were tested
216 by Simultaneous Thermal Analyzer (NETZSCH STA 449F3). Under a continuous nitrogen
217 atmosphere of 20 ml/min, the precisely weighed samples were loaded into a crucible and heated from
218 30 °C to 800 °C at a constant heating rate of 10 °C/min. The evolution of mass loss and heat flow

with temperature is reflected by the thermogravimetric (TG) and differential scanning calorimetry (DSC) curves to determine the thermal stability of NC reinforced LC^3-ECC.

2.4.5. Micromorphology observation

To further observe the microstructural characteristics of NC reinforced LC^3-ECC, the samples were taken from the fracture location of tensile tested specimen and were observed by SEM setup of Thermo scientific Apreo 2S. The samples of size up to 1 cm^3 were cut and polished, followed by gold spraying treatment of their test planes prior to SEM observation. The bonding position of PVA fibres to matrix was investigated by observing the microstructural features and fibre morphology. Microscopic elements of all mixtures were analysed by energy dispersive spectrometry (EDS) mapping analysis using BRUKER XFLASH 6T/60.

2.4.6. Mercury intrusion porosimetry test

MIP tests were conducted to obtain the pore structure characteristics of NC reinforced LC^3-ECC using an AutoPore IV 9500 Hg-porosimeter with pressure range of up to 330 MPa. Tested samples were collected from the previous mechanical experiments and the measurable pore size ranged from 500 μm to 0.005 μm.

3. Results

3.1. Rheology behaviour

3.1.1. Shear stress-time curves

Fig. 7 shows the shear stress evolution with shear time of all mixtures. It can be seen that the shear stress exhibits a tendency to increase and then decrease with shear time, which is a rheological characteristic of cementitious materials. The maximum value of the shear stress in the curve is the static yield stress for the mixtures, meaning the critical stress required to start the flow of the mixture from a stationary state [48]. The free water content, flocculation of the particles, and the hydration process in the mixture are the main factors affecting the static yield stress [49,50]. According to the calculations the static yield stresses of N0, N5, N10, N15 and N20 are 533.0 Pa, 1044.2 Pa, 1183.8 Pa, 1264.7 Pa and 1437.5 Pa, respectively. Obviously, the static yield stresses of the mixes increased significantly with the increase of NC replacement rate. This is due to the reduction in free water content within the fresh mixture, which can be attributed to the agglomeration of nanoparticles and the increase of adsorbed water on the NC particle surface with large specific surface area [51,52].

Furthermore, an increase in the water requirement of the mixture has been observed to enhance the static yield stress with an escalation in the NC replacement ratio.

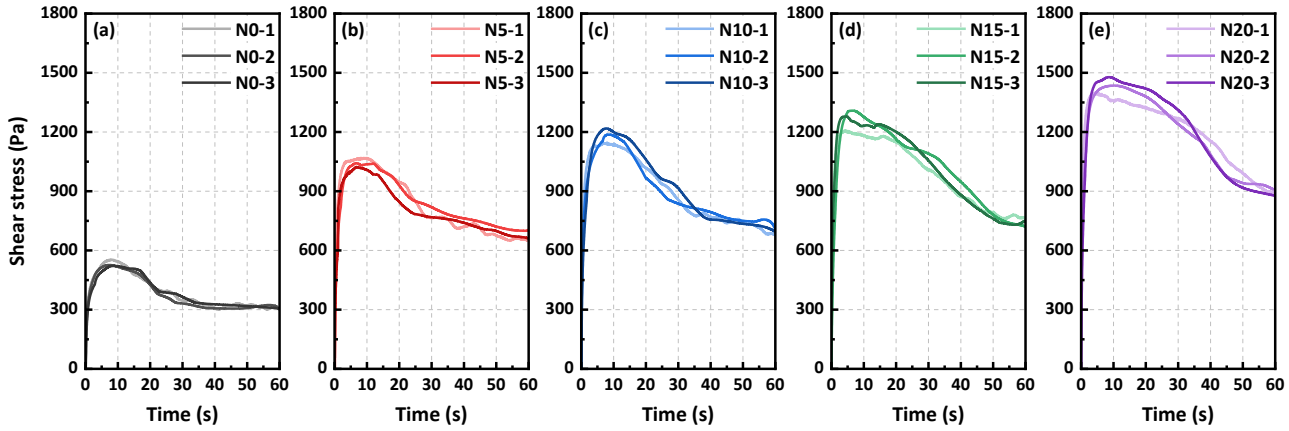

Fig. 8. Shear stress variation with shear time of all mixtures: (a) N0; (b) N5; (c) N10; (d) N15; (e) N20.

3.1.2. Rheological properties

Fig. 9 displays the shear stress-time variation of all mixtures. According to the modified Bingham model (see Eq. (10)) [53], the relationship between the derived yield stress and shear rate can be fitted based on experimental data from three tests. The fitted parameters can be expressed as τ_d and η values of fresh mixtures.

$$\tau = \tau_0 + \eta\dot{\gamma} + c\dot{\gamma}^2 \quad (10)$$

where τ_0 is the corresponding τ_d of fresh mixture.

The fitted data are collated to obtain the rheological properties of NC reinforced LC^3-ECC, as summarised in Table 4. The goodness of fit (R^2) of all mixtures reaches more than 0.8, which can indicate that the relationship between shear stress and shear rate regression is well fitted under modified Bingham model. It can be seen from the curves that the rate of increase in shear stress also shows an improvement as the shear rate increases. This is not only due to the water absorption of by the high specific surface area of NC, but also possibly due to the resistance created by fibre entanglement during the mixing process, which will need to be investigated in further experiments. Fig. 10 shows the dynamic yield stress and plastic viscosity of NC reinforced LC^3-ECC. Overall, the dynamic rheological properties are increased by NC incorporation. The LC^3-ECC with 5%–20% NC replacement of limestone powder increases by 13.3%–54.3% and 12.8%–59.6% in dynamic yield stress and plastic viscosity compared to that of N0, respectively. The plastic viscosity exhibits greater

variability than the dynamic yield stress. In comparison to N5, the dynamic yield stresses of N10, N15 and N20 increase by 13.0%, 26.1% and 36.2%, respectively. Correspondingly, the plastic viscosities of counterparts appear to increase by 12.5%, 29.9% and 41.5%, respectively. It is noteworthy that the enhanced rheological characteristics facilitate the utilisation of cementitious materials in additive manufacturing with superior constructability. Furthermore, the augmented plastic viscosity offers a degree of benefit to the fibre dispersion [40], thereby enabling a concurrent optimisation of both the mechanical strength and deformability of the LC^3-ECC with NC.

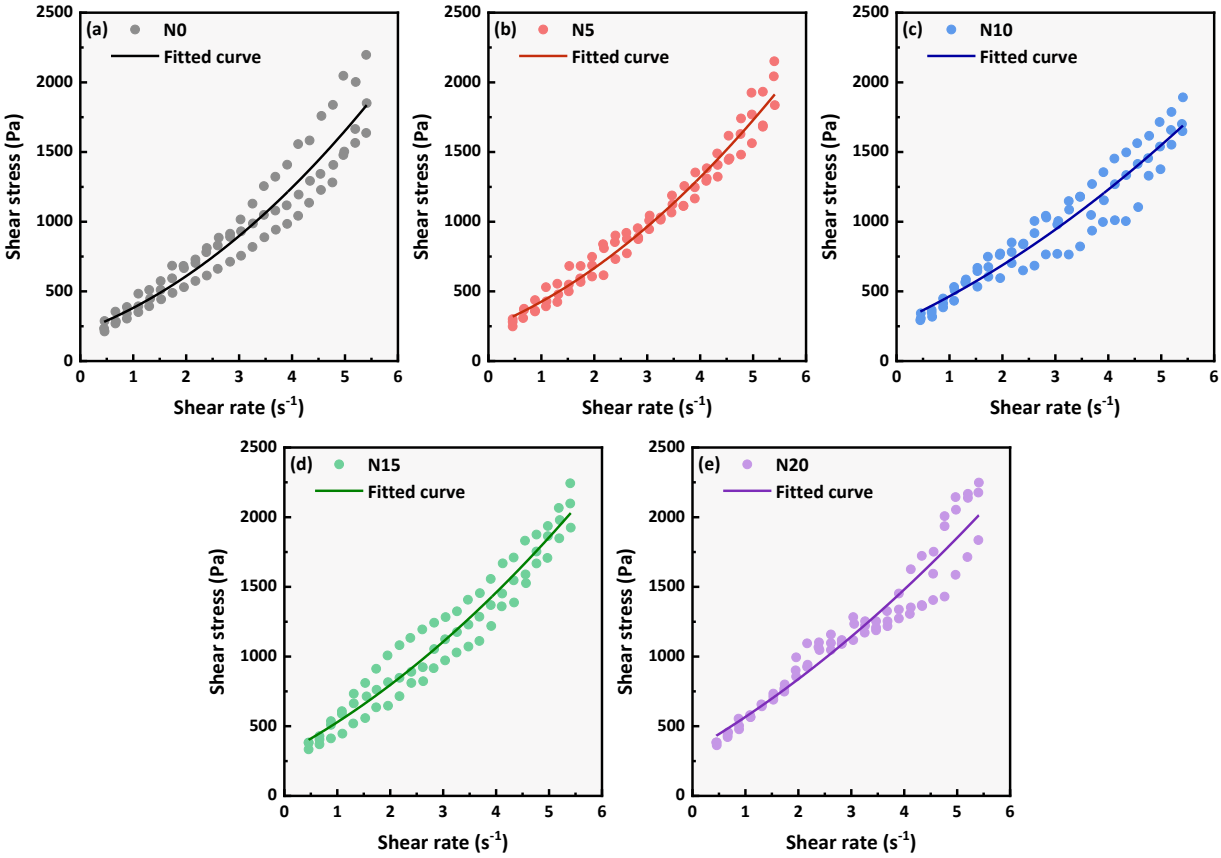

Fig. 9. Shear stress-rate variation of all mixtures: (a) N0; (b) N5; (c) N10; (d) N15; (e) N20.

Table 4 Rheological properties of NC reinforced LC^3-ECC.

Mixture type	τ_s (Pa)	Fitted equation	τ_d (Pa)	η (Pa.s)	R^2
N0	533.0 ± 13.7	$\tau = 213.1 + 138.6\dot{\gamma} + 29.9\dot{\gamma}^2$	213.1	138.6	0.9083
N5	1044.2 ± 18.7	$\tau = 241.5 + 156.3\dot{\gamma} + 28.3\dot{\gamma}^2$	241.5	156.3	0.9712
N10	1183.8 ± 29.1	$\tau = 273.0 + 175.8\dot{\gamma} + 15.9\dot{\gamma}^2$	273.0	175.8	0.9104
N15	1264.7 ± 42.3	$\tau = 304.5 + 203.0\dot{\gamma} + 21.4\dot{\gamma}^2$	304.5	203.0	0.8408
N20	1437.5 ± 31.9	$\tau = 328.9 + 221.2\dot{\gamma} + 16.7\dot{\gamma}^2$	328.9	221.2	0.9263

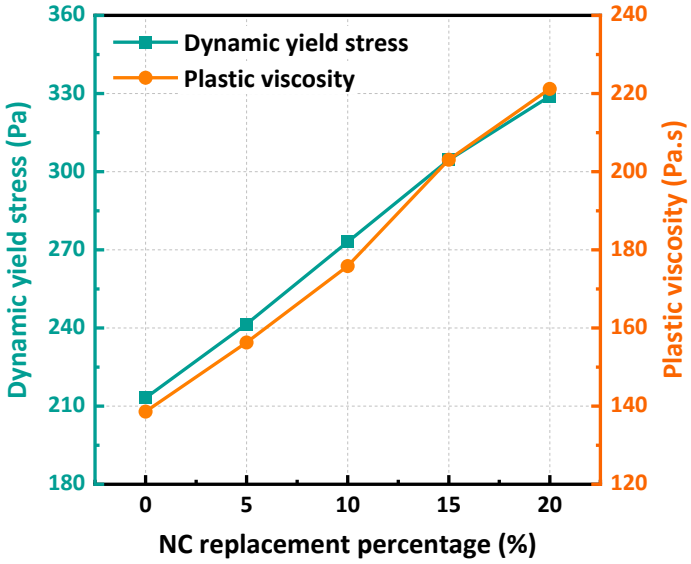

Fig. 10. Dynamic yield stress and plastic viscosity of LC^3-ECC reinforced by NC of different replacement percentages.

3.2. Compressive and flexural strength

Fig. 11 depicts the compressive and flexural strength variation of LC^3-ECC reinforced by NC with different replacement percentages. Overall, the compressive and flexural strengths both shows increasing and then decreasing trends with the growth of NC replacement rate. These two strengths of N5 are the highest in the all mixtures, while the compressive and flexural strength increase by 15.0% and 11.3% compared to that of N0. It can be demonstrated that a NC replacement rate of between 5% and 15% has the effect of enhancing the strength of LC^3-ECC. Nevertheless, at a NC replacement percentage of 20%, the strength of LC^3-ECC will be inferior to that of the reference mixture (N0). At the physical level, some of the NC can be used as ultra-fine micro-aggregate to fill the voids around the binder particles and reduce the defect size inside the matrix in order to enhance the strength by increasing the ECC compactness [30]. The reduction of mechanical properties caused by excessive NC incorporation can be attributed to two aspects. On the one hand, excessive NC incorporation will rapidly fuse with water, reducing the area and probability of contact between various binder ingredients and water which affects the hydration process [54]. On the other hand, the agglomeration of excessive NC weakens the filling effect and affects the chemical reaction properties [55]. Nevertheless, the effect of NC incorporation on flexural strength is significantly greater than that on compressive strength of LC^3-ECC.

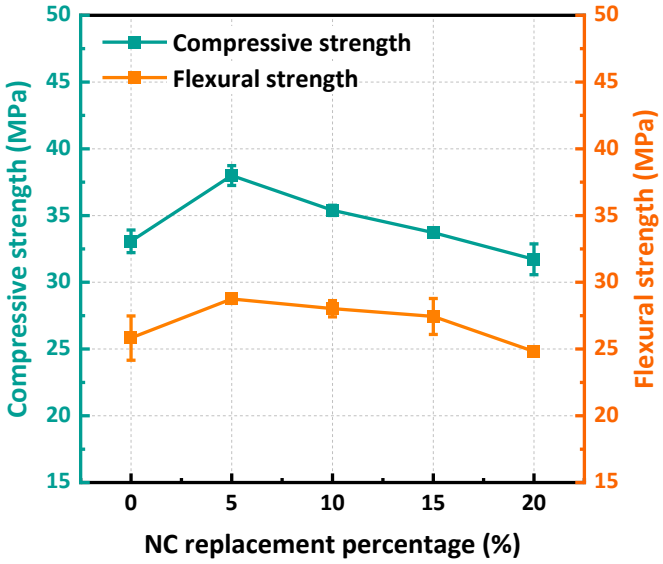

Fig. 11. Compressive and flexural strength of LC^3-ECC reinforced by NC of different replacement percentages.

3.3. Uniaxial tensile behaviour

3.3.1. Tensile characteristics

Fig. 12 illustrates the uniaxial tensile stress-strain curves and the damage morphology in the tensile zone of NC reinforced LC^3-ECC. It is evident that the curves of all mixtures show a stage of fluctuating change after a linear rise, known as the strain hardening stage. In this stage, the fibres mainly play a bridging role to retard the increase in crack width and form a multiple cracking phenomenon [3,56]. Afterwards, the tensile stress exceeds the fibre bridging stress at a certain position causing the ultimate damage of the tested specimen, which is reflected in an instantaneous drop in tensile stress. A clear distribution of multiple cracks can be observed from the tensile damage pattern, and the final fracture location within the tensile region is valid for testing. It has been demonstrated that an increase in the duration of the strain hardening phase is accompanied by a proportional increase in the number of cracks and a decrease in crack width. The matrix properties are the critical factors affecting tensile behaviour when the same dosage of PVA fibres is used. It can be observed that the incorporation of NC resulted in a slight deterioration in the tensile behaviour of LC^3-ECC. It is worth mentioning that the crack width in the tensile region decreased and some tiny cracks could not be observed due to unloading at the end of the tensile test, but the surface cracks remained at the micro scale in all the specimens which is beneficial for the mechanical and long-term properties of the LC^3 based material.

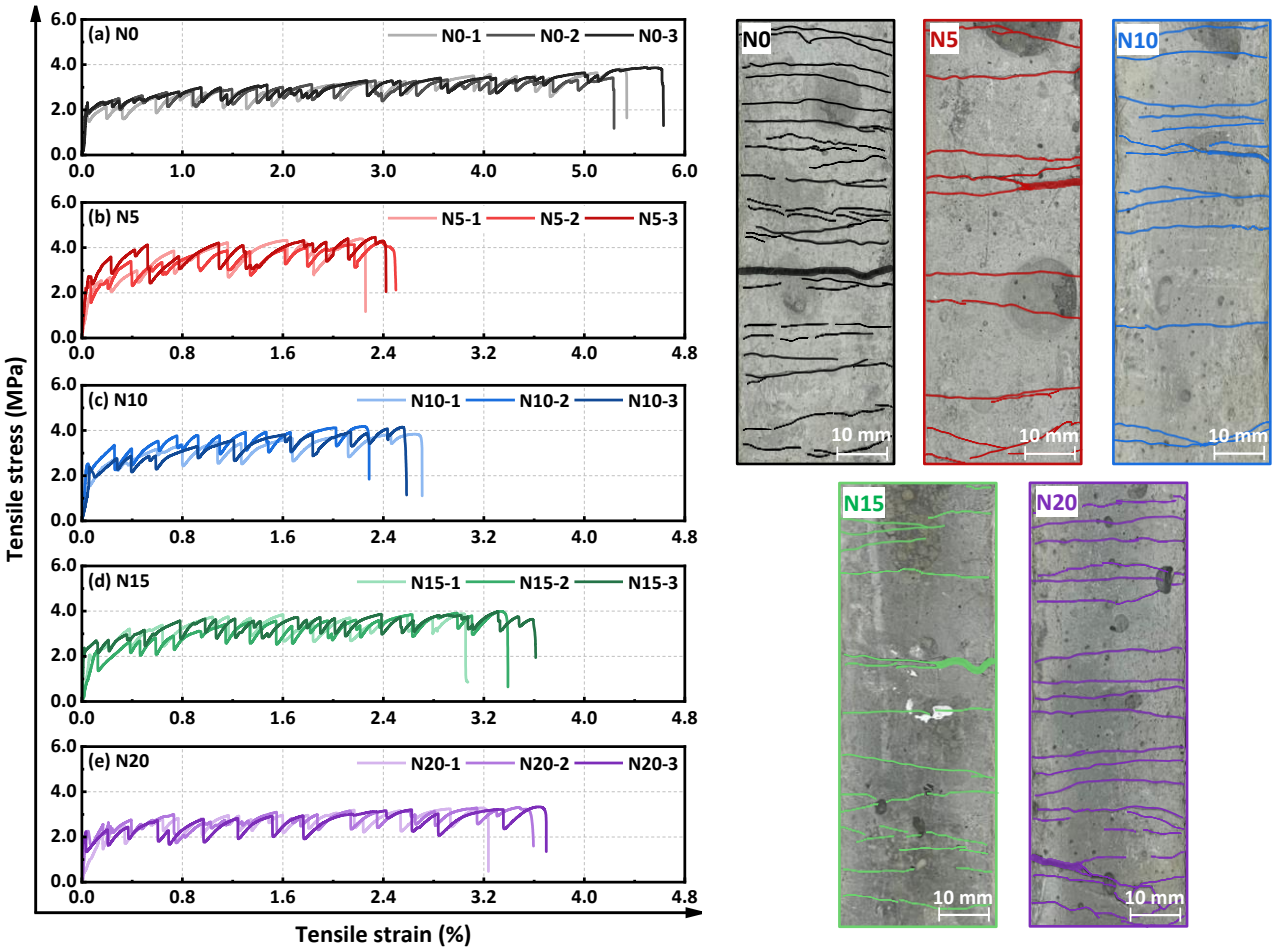

Fig. 12. Tensile stress-strain curves and failure patterns of NC reinforced LC^3-ECC.

Microscopic examination of the tensile cracks reveals two types of PVA fibre pattern, fibre bridging and failure, as shown in Fig. 13. In the initial stage of crack propagation, the PVA fibres de-bond from the matrix and slip to retard crack width propagation. The fibres perform a bridging function and absorb and transmit part of the tensile stress, see Fig. 13a. Subsequently, the fibres are destroyed successively when the stress continually increases, see Fig. 13b. PVA fibres with short anchorage lengths across the crack are pulled out of the matrix, while those with longer anchorage lengths are more likely to rupture [57]. The damage patterns result in the loss of the fibre bridging ability and the extended crack suddenly enlarges, leading to the complete destruction of the tensile tested specimen. Thus, fibre bridging effect at different crack locations is the main contributor to the formation of multiple cracking phenomenon for NC reinforced LC^3-ECC. In the strain hardening phase of the tensile curves shown in Fig. 12, fibre slippage occurred as the stress increased, whereas fibre breakage or pull-out happened as the tensile stress decreased. Therefore, fibre-to-matrix interactions are an important factor affecting the tensile behaviour of NC reinforced LC^3-ECC.

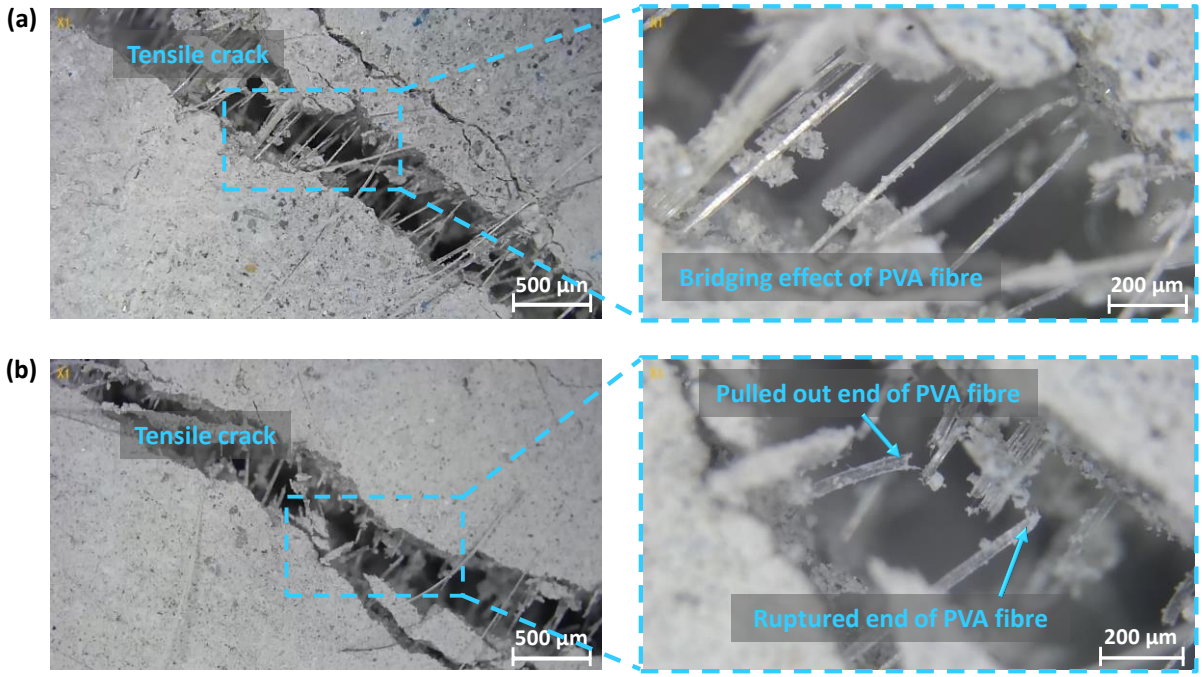

Fig. 13. Fibre appearance at the crack position: (a) bridging effect of PVA fibre; (b) pulled out and ruptured PVA fibre.

3.3.2. Tensile properties

Based on the tensile stress-strain curves, the tensile properties of NC with different replacement rates reinforced LC^3-ECC are illustrated in Fig. 14. The first cracking strength and tensile strength are increase and then decline with increasing NC replacement percentage. Correspondingly, the tensile strain capacity shows an opposite trend, which firstly decreases and then increases. The tensile strength of N5 is the highest of all mixtures, while the tensile strain capacity is the worst but still more than 2%. Compared to N0, the tensile strength of N5, N10, N15 and N20 increase by 18.1%, 9.5%, 6.8% and –10.5%, respectively. The tensile strain capacity of NC reinforced LC^3-ECC reduce by 36.8%–57.3% than that of N0. The incorporation of nanomaterials results in enhanced tensile strength, but concurrently the fibre bridging ability is weakened. Partial filling of tiny pores within the matrix by NC is not conducive to fibre slippage, leading to relatively rapid crack expansion manifested as a reduction in strain-hardening capacity. Meanwhile the cement hydration reaction promoted by NC may contribute to an increasing adhesion of the fibre matrix, again adversely affecting the tensile deformation capacity [24]. Nevertheless, all mixtures exhibit significant tensile toughness are more than 200 times that of plain concrete which tensile strain capacity of about 0.01% [3]. Moreover, the N15 mixture has a higher tensile strength than N0 while the tensile strain of N15 reaches 3%.

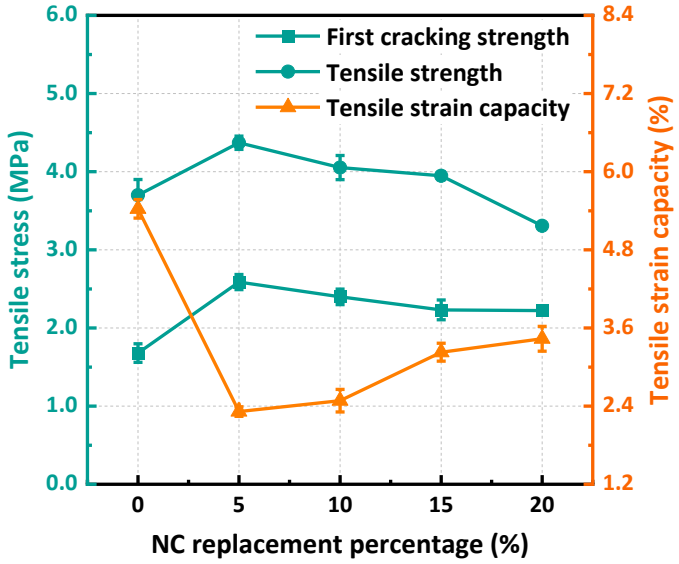

Fig. 14. Tensile properties of LC^3-ECC reinforced by NC of different replacement percentage.

3.4. Micromechanical analysis

3.4.1. Fibre bridging stress-crack opening curves

Fig. 15 displays the fibre bridging stress-crack opening displacement curves of all mixtures, which correspond σ_0 and δ_0 are listed in Table 5. The interfacial bonding properties of the fibres to matrix are primarily reflected in the chemical bonding action and physical anchoring capacity between them [47]. The increasing stage of tested curve indicates that the stress required to overcome the fibre-matrix bonding action during the tensile process is increasing, and that the bond strength generated between them is also improving. In LC^3-ECC without NC incorporation, the value of σ_0 is the highest of all mixtures and thus exhibits a significant strain-hardening capacity in Section 3.3.1. It can be observed that the higher fibre bridging stresses typically result in larger corresponding crack opening widths. It is postulated that this phenomenon occurs in consequence of the fact that fibre slippage necessitates the application of greater stresses in comparison to cracking [58]. The fibre bridging stress and crack opening displacement of NC reinforced LC^3-ECC decreased by 11.1%–18.5% and 3.8%–36.7%, respectively, with the most notable decline observed in N5. It is attributed to the stronger bonding and friction effect which reduces the occurrence of fibre bridging resulting in lower crack controlled capacity [3], which is the main reason for the poorer tensile strain capacity for N5. Furthermore, the alteration in the crack opening width is more pronounced in comparison to the fibre bridging stress, which can be attributed to the consistent incorporation of PVA fibres and the predominant influence of NC on matrix properties.

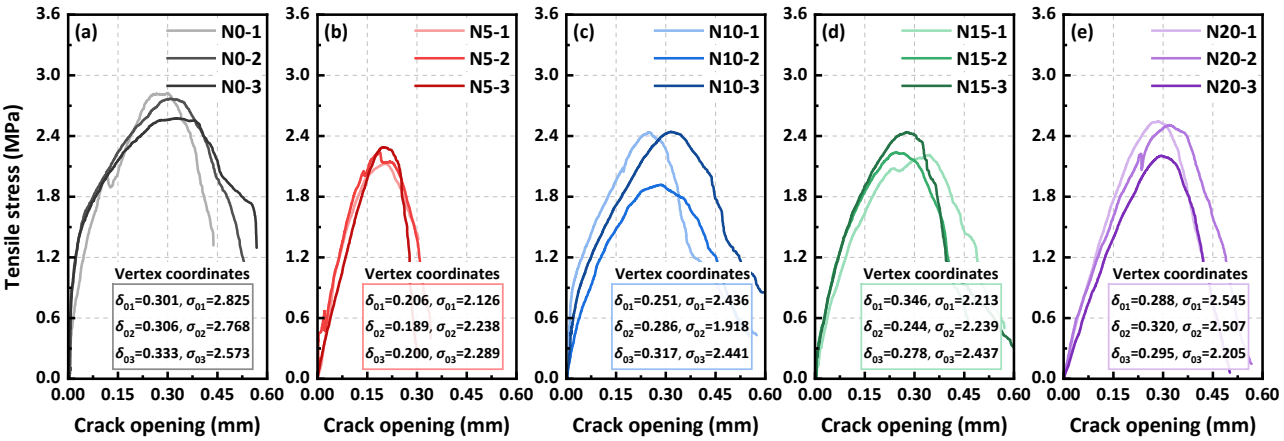

Fig. 15. Tensile stress-crack opening displacement curves with vertex coordinates (δ_0, σ_0) of all mixtures: (a) N0; (b) N5; (c) N10; (d) N15; (e) N20.

Table 5 Results of single crack uniaxial tension.

Mixture type	Fibre birding stress, σ_0 (MPa)	Corresponding crack opening, δ_0 (mm)
N0	2.722 ± 0.108	0.313 ± 0.014
N5	2.218 ± 0.068	0.198 ± 0.007
N10	2.265 ± 0.245	0.284 ± 0.027
N15	2.296 ± 0.100	0.289 ± 0.043
N20	2.419 ± 0.152	0.301 ± 0.014

3.4.2. PSH index calculation

To further evaluate the tensile properties of NC-reinforced LC^3-ECC and whether it satisfies the saturated cracking state, the PSH index is invoked to quantitatively judge the two criterion completion criteria of all mixtures [3]. According to the strength and energy criteria mentioned in Section 2.4.2, the PSH indices are calculated as follows [3,59]:

$$PSH\ \ strength = \frac{\sigma_0}{\sigma_{fc}} \tag{11}$$

$$PSH\ \ energy = \frac{J_b^{'}}{J_{tip}} \tag{12}$$

The experimental results obtained based on fracture toughness testing of the matrix are recorded in Table 6. Then, the value of J_{tip} is determined by combining the elastic modulus measured from the tensile test of mortar matrix, and the calculation of $J_b^{'}$ is obtained by integrating the σ_0-δ_0 curves. Based on the obtained parameters, the PSH indices are calculated and the relevant data are summarised in Table 7. In accordance with the micromechanical model, the presence of both $\sigma_0/\sigma_{fc} \geq 1$ and $J_b^{'}/J_{tip} \geq 1$ is indispensable for the occurrence of multiple cracking. Nevertheless,

experimental evidence has demonstrated that conditions $\sigma_0/\sigma_{fc} \geq 1.3$ and $J_b'/J_{tip} \geq 2.7$ are the more conservative means of achieving stable tensile strain hardening due to the quality fluctuation of raw materials [60]. Overall, all mixtures satisfy the PSH energy condition. For the PSH strength condition, only N5 is not satisfied with a value of 1.05 which shows the lowest strain hardening behaviour. This phenomenon can be attributed primarily to the strong intermolecular forces that exist between the fibres and matrix. The incorporation of NC in LC^3-ECC resulted in a more pronounced enhancement in PSH energy values in comparison to PSH strength values, indicating that NC is relatively more responsive to tensile energy.

Table 6 Fracture toughness of NC reinforced LC^3 mortar.

Mixture type	Mass (g)	Peak load (N)	Fracture toughness, K_m (MPa·m$^{1/2}$)
N0	486.3 ± 5.229	931.7 ± 66.87	0.444 ± 0.032
N5	481.4 ± 3.061	824.3 ± 40.10	0.393 ± 0.019
N10	485.4 ± 6.708	803.3 ± 20.69	0.383 ± 0.010
N15	482.5 ± 4.609	849.3 ± 27.23	0.405 ± 0.013
N20	481.5 ± 8.859	890.5 ± 74.17	0.424 ± 0.035

Table 7 PSH calculation of NC reinforced LC^3-ECC.

Mixture type	σ_{fc} (MPa)	*PSH strength*	J_{tip} (J/m^2)	J_b' (J/m^2)	*PSH energy*
N0	1.419	1.919 ± 0.076	22.33	203.5	9.113 ± 0.934
N5	2.110	1.051 ± 0.032	12.53	159.1	12.70 ± 1.188
N10	1.640	1.381 ± 0.150	12.86	200.9	15.62 ± 1.201
N15	1.480	1.552 ± 0.068	15.03	206.2	13.72 ± 0.872
N20	1.318	1.836 ± 0.116	16.19	284.0	17.54 ± 0.791

3.5. Phase analysis

Fig. 16 shows the XRD patterns of NC reinforced LC^3-ECC paste at different curing ages. The increase in the diffraction peak intensity of calcium carbonate implies the incorporation of NC granules. During the first 7 d of curing age (see Fig. 16a), the diffraction peak intensity of calcium hydroxide (CH) in N20 is consistently lower than that of N0, indicating that the incorporation of NC consumes a certain amount of CH during the reaction process [34]. At curing age of 1 d, the contents of hemicarboaluminate (Hc) in N0 and N20 have little difference, while the diffraction peak intensity of Hc in N20 is greater than that of N0 at 3 d and 7 d. This indicates that the carbon-aluminate reaction occurs gradually after more than 24 h of curing age. NC can react with C3A and C4AF and promote early hydration so that Al cations are mainly immobilised in the carbon-aluminate products [34,61].

As shown in Fig. 16b, the diffraction peak intensities of the CH in all mixtures are significantly reduced, whilst N5 has the highest diffraction intensity of the main calcium carbonate peak. Due to the amorphous characteristics of non-crystalline components such as calcium-silicate-hydrate (C-S-H) gels, they have no specific diffraction peaks and the remainder of the carbonate-based hydration products may be hidden near the diffraction peaks of all calcite [62]. Moreover, NC is capable of reacting with larger Ca^{2+} precipitated from cement and OH^- from the cement hydration products, forming many nucleation sites on the surface of calcium ions and contributing to C-S-H gels generation [24,63].

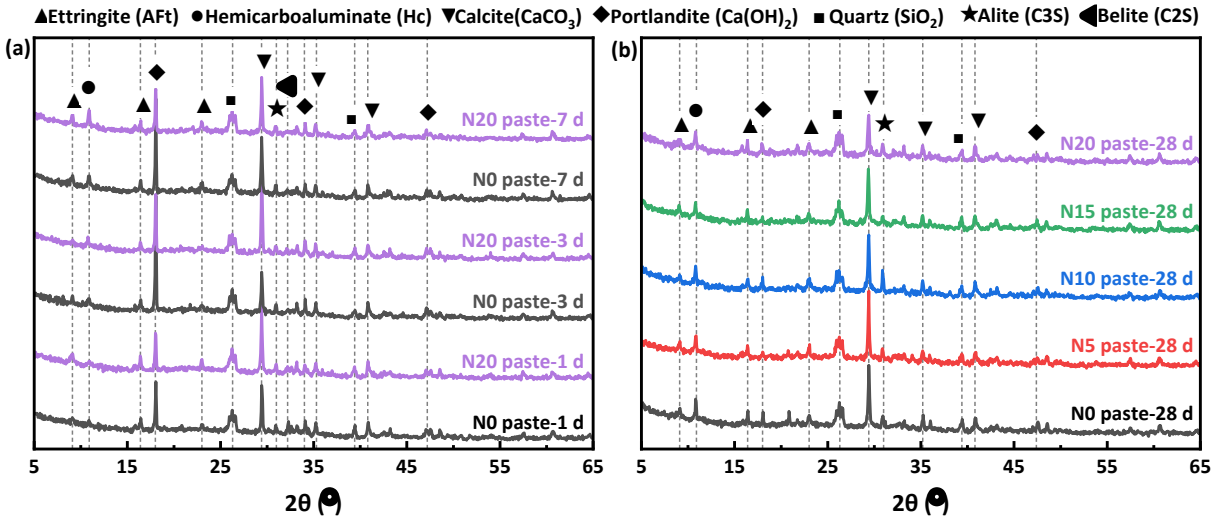

Fig. 16. XRD patterns of NC reinforced LC^3-ECC paste.

Fig. 17 displays the TG and DSC curves of LC^3-ECC with NC of different replacement percentages at elevated temperatures. When the temperature increases from room temperature to 800 °C, the weight loss of N0, N5, N10, N15 and N20 obtained from TG curves is 14.57%, 15.00%, 13.47%, 12.49% and 10.92%, respectively. In the DSC curves, only one obvious exothermic peak is observed around 700 °C for the decomposition of calcium carbonate without the decomposition of CH. This indicates that the CH in the NC reinforced LC^3-ECC is fully reacted to form carbonate products. When the NC replacement rate is not more than 10%, the mass loss is not changed significantly before the temperature reaches 200 °C indicating that the free water contents in the composites are similar. The mass loss of N15 and N20 before 200 °C is obviously lower than that of the other mixes, showing that the content of free water in them is significantly reduced due to the excessive incorporation of NC. Above 200 °C, the hydration products in the ECC decompose

successively and the decrease in mass loss is mainly due to the evaporation of bound water and the escape of CO_2 [56]. The total mass loss of N5 is the largest in all mixtures, indicating that the content of decomposed hydration products in the matrix is the highest, consistent with the XRD results showing the highest intensity of carbonate-based phases of N5.

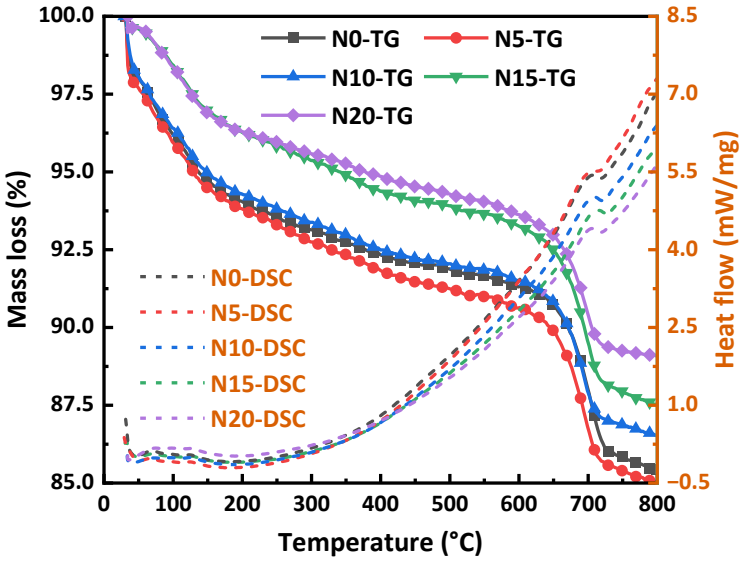

Fig. 17. TG and DSC curves of NC reinforced LC^3-ECC.

3.6. Micromorphology appearance

As seen in Fig. 18, the microstructure and fibre morphology within the matrix are observed using SEM. Matrix fragments and scratches can be clearly seen on the surface of the fibre (Fig. 18a), which indicates that the fibres can effectively bond with the matrix and improve the toughness of the composites. The fibre morphology observed in Fig. 18b corroborates the two damage modes of fibres described in Section 3.3.1, i.e. fibre rupture and fibre pull-out. The pull-out ends of the PVA fibres are relatively flat and not much different from the initial fibre ends, where there are almost no matrix fragments. The ruptured ends of PVA fibre are spiky and a significant reduction in diameter can be observed. Herein, the rupture behaviour of PVA fibres indicate a stronger bond to the matrix [64]. Additionally, the presence of conspicuous voids at the site of damaged fibres bonded to the matrix is evident (Fig. 18c), which are attributed to fibre slippage and the subsequent spalling of surrounding fragments in weak zones. The presence of scratches on the fibre surface to varying degrees indicates that the PVA fibres are able to slip effectively, which is beneficial to the tensile properties of NC reinforced LC^3-ECC.

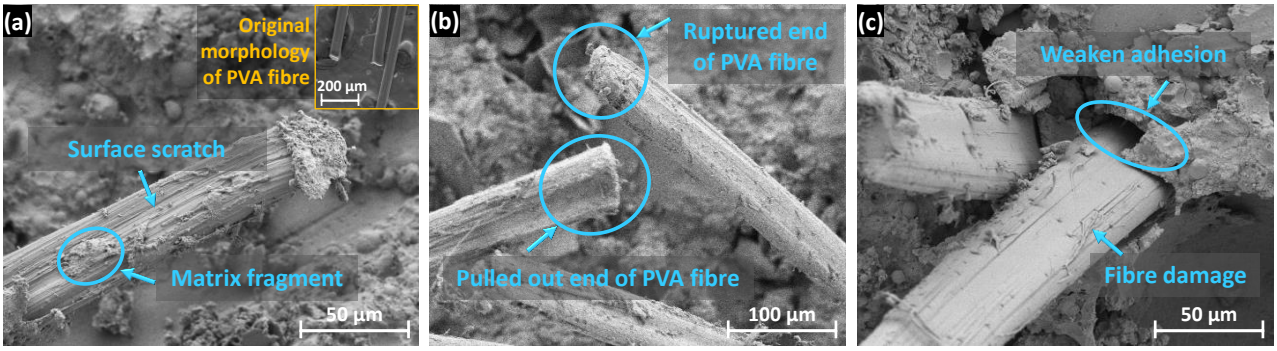

Fig. 18. SEM images of NC reinforced LC^3-ECC: (a) PVA fibre surface; (b) the end of fibre with different failure patterns; (c) fibre-to-matrix bonding position.

Fig. 19 displays the BSE images with EDS map for major elements of all mixtures, and the major element contents are summarised in Table 8. Of these, the C element content is unreliable because the fixing adhesive of the samples contained a portion of C during the test. Element Ca derived from calcium hydroxide, calcium carbonate and C-S-H gels has the highest atomic percentage in the N5. The concentration of Si element in the EDS map represents the quartz sand, and the position of the element dispersion is more representative of unreacted ingredients and C-S-H gels. The origin of element Al is partly provided by C-A-S-H gels produced by hydration reactions apart from that contained in fly ash and calcined clay, whereas the percentage of element Al decreases gradually with increasing NC replacement ratio. Hence, the distribution of O, Ca, Si and Al elements can be observed uniformly in the matrix except for the location of fibres and aggregates. Moreover, the PVA fibres are effectively embedded in the matrix. The hydration products and part of the raw materials are uniformly distributed and effectively bonded to the ingredients in the NC reinforced LC^3-ECC.

Table 8 Spectrum analysis for different samples.

Element	N0		N5		N10		N15		N20	
	Weight /%	Atomic /%	Weight /%	Atomic /%	Weight /%	Atomic /%	Weight /%	Atomic /%	Weight /%	Atomic /%
C	15.73	24.88	19.71	29.97	25.73	37.20	23.29	34.35	16.05	25.46
O	42.34	50.30	43.53	49.67	40.96	44.45	41.81	46.29	40.96	48.77
Ca	18.11	8.59	18.87	8.60	12.62	5.47	14.55	6.43	17.31	8.23
Si	16.77	11.35	10.70	6.96	12.35	7.64	11.98	11.98	16.71	11.34
Al	6.29	4.43	6.65	4.50	7.18	4.62	7.20	4.73	7.88	5.57

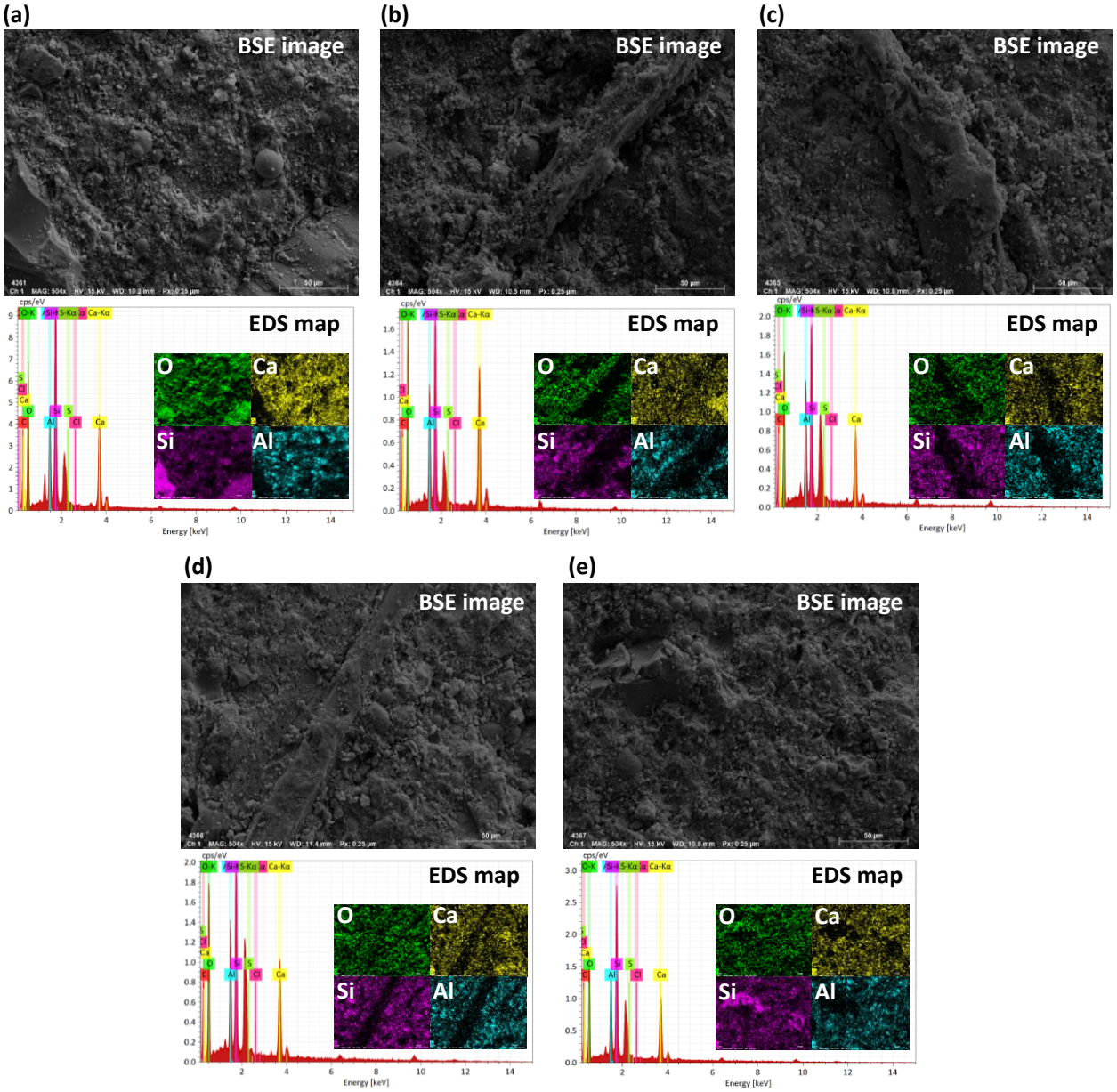

Fig. 19. EDS map based on BSE images of all mixtures: (a) N0; (b) N5; (c) N10; (d) N15; (e) N20.

3.7. Pore structure characterization

Fig. 20a and b depict the pore size distribution of LC^3-ECC reinforced by NC with replacement limestone powder ratio of 0, 5% and 20%. According to the previous research [56], the pores can be can be classified into four groups depending on the diameter: gel and meso pores (<100 nm), middle capillary pores (100–1000 nm), large capillary pores (1000–10000 nm), and macro pores (>10000 nm). The corresponded volume percentages of pore with different sizes are calculated in the Fig. 20c. Based on the tested results, the incorporation of NC has almost little effect on the total porosity of LC^3-ECC, while it is influential on the distribution of pore sizes. When NC with a replacement rate of 5% is incorporated, the percentage of capillary pores decreases due to the ability of NC in filling

the internal pores while there is an increase in the percentage of gel, meso and macro pores in the specimen. The nucleation of NC promotes the generation of denser C-S-H gels and increases the content of prismatic CH [29]. The refinement of CH leads to the overlapping of high-density C-S-H gels and others products, which increase the amount of gel and meso pores. However, when excessive NC is added to the matrix, only the percentage of gel and meso pores decreased whereas the percentage of pores with diameters lager than 100 nm all raised. Among them, the percentage of medium capillary pores of N20 is still less than that of N0. Thus, the incorporation of NC in LC^3-ECC mainly affects the proportion of macro pores, whilst the variation of NC content is closely related to the proportion of middle capillary pores. The consistency of the change trend in middle capillary pores proportion with the mechanical strength of LC^3-ECC is essential for its macro performance.

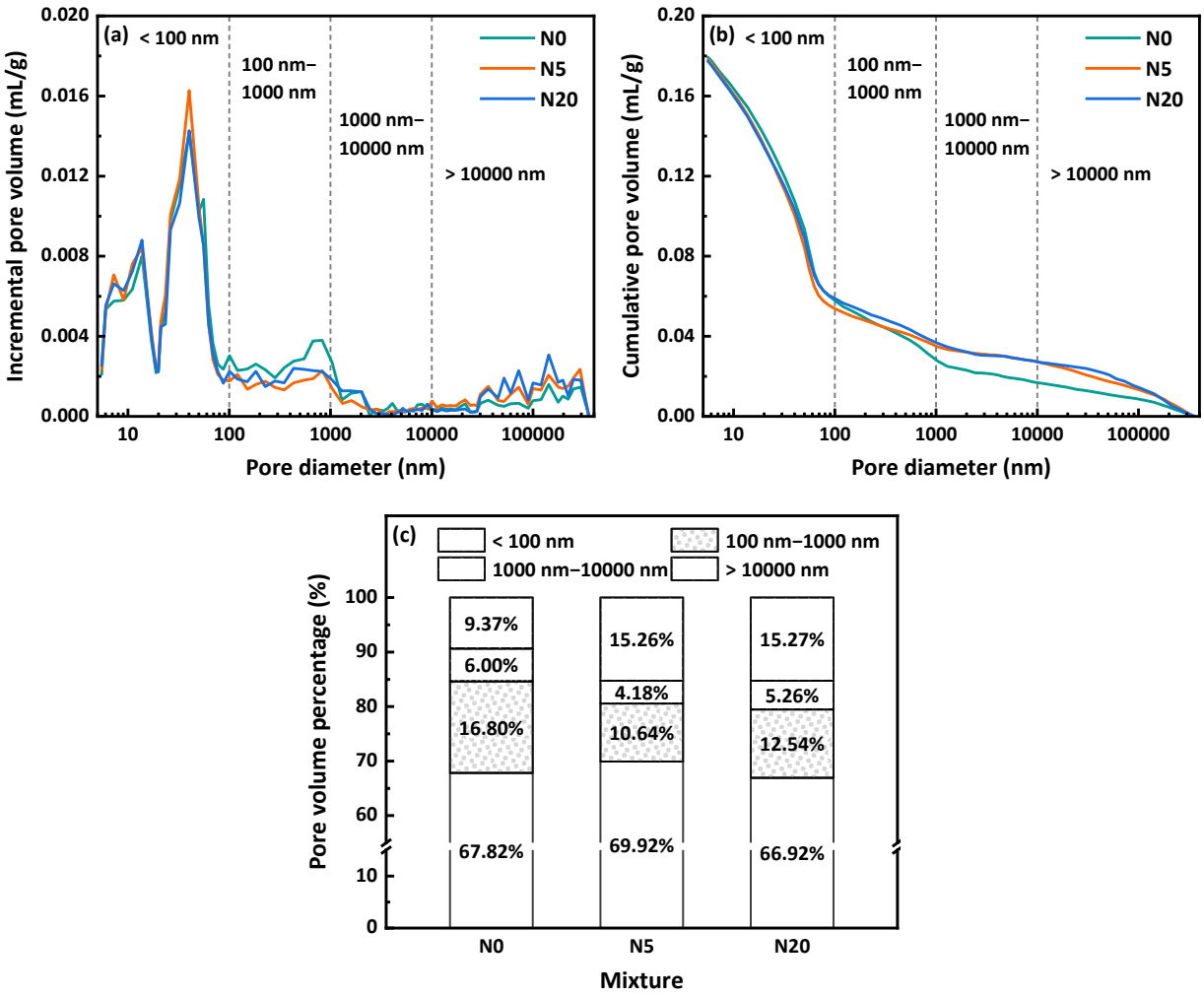

Fig. 20. Pore size distribution of NC reinforced LC^3-ECC: (a) incremental pore volume; (b) cumulative pore volume; (c) pore volume percentage of different sizes.

4. Discussion

As one of the commonly used nano-reinforcing ingredients in cementitious materials, NC results in the enhancement of the mechanical strength for LC^3-ECC when incorporated in the proper amount, and the effect of which is shown schematically in Fig. 21. During the hydration process, NC could react with C3A and hydroxide ions inside the matrix (see Fig. 16) as well as forms nucleation sites on the micro-sized limestone powder, which increases the content of high density C-S-H gels [61,63]. Moreover, NC particles can fill in the cavities of interfacial transition zone between the C-S-H gels and aggregates [65], refining the pore size distribution of the matrix (see Fig. 20) and allowing a more uniform distribution of hydration products [24]. The filling and hydration promotion effects of NC both resulted in an improvement in the mechanical properties of LC^3-ECC. When excessive amounts of NC are incorporated, the NC particles become agglomerated and cannot effectively perform the filling effect and chemical reaction, resulting in reduced flowability. Moreover, it also influences on the bridging behaviour of the PVA fibres in LC^3-ECC. The effect of NC on the hydration reaction and microstructure reduces the matrix toughness and fibre-to-matrix bonding strength of LC^3-ECC, as mentioned in Section 3.4. On this basis, ECC materials need to be judged according to design criteria to measure whether they meet the design requirements. Therefore, the NC has an integrated effect on the fresh/mechanical properties and microstructure of the LC^3 matrix.

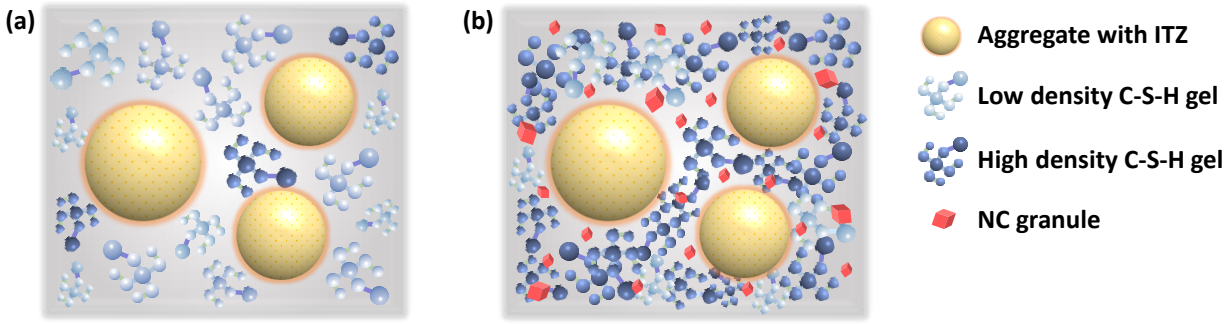

Fig. 21. Schematic representation of microstructure of LC^3-ECC: (a) without NC, (b) with NC.

The effect of NC replacement of limestone powder on LC^3-ECC is analysed in combination with fresh and mechanical properties, as presented in Fig. 22. Therein, all values of N0 are set to 1.0 while the results of LC^3-ECC reinforced by NC are adjusted according to the value of N0. The incorporation of NC increases the static/dynamic yield stress and plastic viscosity of the fresh mixtures, resulting in a decrease in the rheological properties of LC^3-ECC. This can be attributed to the reduction of free

water content inside the matrix due to the particle size grade of NC. Simultaneously, NC is bonded to the hydration parameters inside the matrix, forming a three-dimensional lattice that improves the internal interfaces and the overall structure. The NC replacement rate of 5% for LC^3-ECC showed the highest values of all mechanical properties, accompanied by a decrease in the tensile ductility of ECC. The N5 mixture does not satisfy the strength design criteria according to the results mentioned in Section 3.4.2. The N10 and N15 mixes have slightly lower strengths than N5, but both are higher than that of N0. Although the enhancement of NC is not fully realised, there is a combined improvement in the fresh and hardened properties. It is advantageous for the following rapid construction of the LC^3-ECC. Furthermore, N10 and N15 mixtures fulfil the design criteria to a greater extent. However, NC does not fully enhance the mechanical performance of LC^3-ECC when the NC replacement rate exceeds 15% up to 20%, probably due to the agglomeration effect of NC particles resulting in a reduction in the number of actual internal reaction nucleation sites [27]. Therefore, the replacement rate of NC should be maintained at less than 15%. Additionally, an optimal ratio of enhanced strength or ductility should be selected for practical application based on engineering requirements.

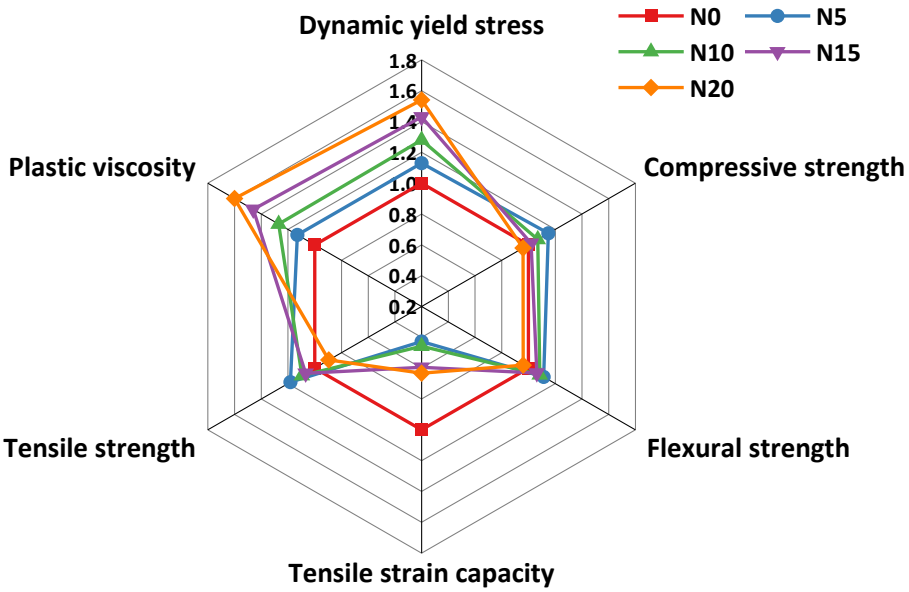

Fig. 22. Properties comparison between LC^3-ECC and NC reinforced LC^3-ECC.

5. Conclusions

This paper systematically investigated the fresh and mechanical properties of LC^3-ECC prepared by replacing limestone powder with NC replacement rate of 0, 5%, 10%, 15% and 20%. The rheological, compressive, flexural and tensile properties of the NC reinforced LC^3-ECC were tested.

Furthermore, the macro performance variations were analysed based on the micromechanical parameters and microstructural characterisation. Based on the experimental results, the specific conclusions are summarised below:

- The static/dynamic yield strength and plastic viscosity of LC^3-ECC increased with increasing NC replacement rate, which is classified by the adsorption of NC on free water and the encapsulation of hydro-molecules by the agglomerated particles. When the NC content was excessive, the change in the rheological properties would affect the practical pouring process of LC^3-ECC.
- The compressive or flexural strength of LC^3-ECC increased and then decreased with the increase of NC replacement rate with a maximum value of N5 mixture, which increased by 15.0% and 11.3% than that of N0, respectively. NC improved the hydration process and refined the microstructure of LC^3-ECC but an excessive incorporation of NC led to its agglomeration, which interfered with the reaction process and resulted in the strength reduction.
- For tensile properties, the incorporation of NC improved the initial and ultimate tensile strengths, but the tensile strain capacity decreased considerably even though it still exceeds 2%. The reinforcement of the LC^3-ECC by NC limits the PVA fibre bridging behaviour, leading to a weakening of the controlled ability to crack initiation.
- The incorporation of NC consumes a large amount of CH and promotes the generation of hydration products, as well as contributes to the reduction of the capillary pore distribution of LC^3-ECC. The NC replacement rate of 5% failed to satisfy the design guidelines for ECC although it had the highest mechanical properties. Thus, the NC replacement rate of about 10%–15% was the optimal range for its reinforcement for LC^3-ECC in this work.

Acknowledgements

The authors gratefully acknowledge the financial support by the Liaoning Provincial Natural Science Foundation (2024-MSBA-28), and the Fundamental Research Funds for the Central Universities (N2401001).

References

[1] V.C. Li, C.K.Y. Leung, Steady-State and Multiple Cracking of Short Random Fiber Composites, J. Eng. Mech. 118 (1992) 2246–2264. https://doi.org/10.1061/(asce)0733-

572 9399(1992)118:11(2246).
573 [2] D.Y. Yoo, N. Banthia, High-performance strain-hardening cementitious composites with
574 tensile strain capacity exceeding 4%: A review, Cem. Concr. Compos. 125 (2022) 104325.
575 https://doi.org/10.1016/j.cemconcomp.2021.104325.
576 [3] V.C. Li, Engineered cementitious composites (ECC) : Bendable concrete for sustainable and
577 resilient infrastructure, Springer, 2019. https://doi.org/10.1007/978-3-662-58438-5.
578 [4] V.C. Li, From micromechanics to structural engineering-the design of cementitous
579 composites for civil engineering applications, J. Struct. Mech. Earthq. Eng. 10 (1993) 37–48.
580 https://doi.org/10.2208/jscej.1993.471_1.
581 [5] C. Lu, J. Yu, C.K.Y. Leung, An improved image processing method for assessing multiple
582 cracking development in Strain Hardening Cementitious Composites (SHCC), Cem. Concr.
583 Compos. 74 (2016) 191–200. https://doi.org/10.1016/j.cemconcomp.2016.10.005.
584 [6] J. Lao, B. Huang, Y. Fang, L. Xu, J. Dai, Strain-hardening alkali-activated fly ash / slag
585 composites with ultra-high compressive strength and ultra-high tensile ductility, 165 (2023)
586 107075. https://doi.org/https://doi.org/10.1016/j.cemconres.2022.107075.
587 [7] D. Shoji, Z. He, D. Zhang, V.C. Li, The greening of engineered cementitious composites
588 (ECC): A review, Constr. Build. Mater. 327 (2022) 126701.
589 https://doi.org/10.1016/j.conbuildmat.2022.126701.
590 [8] N. Shanmugasundaram, S. Praveenkumar, Influence of supplementary cementitious
591 materials, curing conditions and mixing ratios on fresh and mechanical properties of
592 engineered cementitious composites – A review, Constr. Build. Mater. 309 (2021) 125038.
593 https://doi.org/10.1016/j.conbuildmat.2021.125038.
594 [9] K. Scrivener, F. Martirena, S. Bishnoi, S. Maity, Calcined clay limestone cements (LC^3),
595 Cem. Concr. Res. 114 (2018) 49–56. https://doi.org/10.1016/j.cemconres.2017.08.017.
596 [10] M. Hou, D. Zhang, V.C. Li, Material processing, microstructure, and composite properties of
597 low carbon Engineered Cementitious Composites (ECC), Cem. Concr. Compos. 134 (2022)
598 104790. https://doi.org/10.1016/j.cemconcomp.2022.104790.
599 [11] J. Yu, D.K. Mishra, C. Hu, C.K.Y. Leung, S.P. Shah, Mechanical, environmental and
600 economic performance of sustainable Grade 45 concrete with ultrahigh-volume Limestone-

Calcined Clay (LCC), Resour. Conserv. Recycl. 175 (2021) 105846. https://doi.org/10.1016/j.resconrec.2021.105846.

[12] A. Al-Fakih, M. A. Al-Shugaa, M. A. Al-Osta, B.S. Thomas, Mechanical, environmental, and economic performance of engineered cementitious composite incorporated limestone calcined clay cement: A review, J. Build. Eng. 79 (2023) 107901. https://doi.org/10.1016/j.jobe.2023.107901.

[13] H. Zhu, K. Yu, W. McGee, T.Y. Ng, V.C. Li, Limestone calcined clay cement for three-dimensional-printed engineered cementitious composites, ACI Mater. J. 118 (2021) 111–122. https://doi.org/10.14359/51733109.

[14] W. Chen, J. Dang, H. Du, Using low-grade calcined clay to develop low-carbon and lightweight strain-hardening cement composites, J. Build. Eng. 58 (2022) 105023. https://doi.org/10.1016/j.jobe.2022.105023.

[15] Y. Chen, S. He, Y. Zhang, Z. Wan, O. Çopuroğlu, E. Schlangen, 3D printing of calcined clay-limestone-based cementitious materials, Cem. Concr. Res. 149 (2021) 106553. https://doi.org/10.1016/j.cemconres.2021.106553.

[16] W.J. Long, C. Lin, J.L. Tao, T.H. Ye, Y. Fang, Printability and particle packing of 3D-printable limestone calcined clay cement composites, Constr. Build. Mater. 282 (2021) 122647. https://doi.org/10.1016/j.conbuildmat.2021.122647.

[17] L.G. Briendl, F. Mittermayr, A. Baldermann, F.R. Steindl, M. Sakoparnig, I. Letofsky-Papst, I. Galan, Early hydration of cementitious systems accelerated by aluminium sulphate: Effect of fine limestone, Cem. Concr. Res. 134 (2020) 106069. https://doi.org/10.1016/j.cemconres.2020.106069.

[18] D. Jiang, X. Li, Y. Lv, M. Zhou, C. He, W. Jiang, Z. Liu, C. Li, Utilization of limestone powder and fly ash in blended cement: Rheology, strength and hydration characteristics, Constr. Build. Mater. 232 (2020) 117228. https://doi.org/10.1016/j.conbuildmat.2019.117228.

[19] L. Wang, N. Ur Rehman, I. Curosu, Z. Zhu, M.A.B. Beigh, M. Liebscher, L. Chen, D.C.W. Tsang, S. Hempel, V. Mechtcherine, On the use of limestone calcined clay cement (LC^3) in high-strength strain-hardening cement-based composites (HS-SHCC), Cem. Concr. Res. 144

(2021) 106421. https://doi.org/10.1016/j.cemconres.2021.106421.

[20] J. Yu, H.L. Wu, C.K.Y. Leung, Feasibility of using ultrahigh-volume limestone-calcined clay blend to develop sustainable medium-strength Engineered Cementitious Composites (ECC), J. Clean. Prod. 262 (2020) 121343. https://doi.org/10.1016/j.jclepro.2020.121343.

[21] D. Zhang, B. Jaworska, H. Zhu, K. Dahlquist, V.C. Li, Engineered Cementitious Composites (ECC) with limestone calcined clay cement (LC^3), Cem. Concr. Compos. 114 (2020) 103766. https://doi.org/10.1016/j.cemconcomp.2020.103766.

[22] H. Zhu, D. Zhang, T. Wang, H. Wu, V.C. Li, Mechanical and self-healing behavior of low carbon engineered cementitious composites reinforced with PP-fibers, Constr. Build. Mater. 259 (2020) 119805. https://doi.org/10.1016/j.conbuildmat.2020.119805.

[23] A.G. Mehairi, M.M. Husein, Enhancement of cement properties by means of in situ grown nanoparticles, Constr. Build. Mater. 261 (2020) 120496. https://doi.org/10.1016/j.conbuildmat.2020.120496.

[24] Q. Fu, Z. Zhang, X. Zhao, W. Xu, D. Niu, Effect of nano calcium carbonate on hydration characteristics and microstructure of cement-based materials: A review, J. Build. Eng. 50 (2022) 104220. https://doi.org/10.1016/j.jobe.2022.104220.

[25] B. Xi, Y. Zhou, K. Yu, B. Hu, X. Huang, L. Sui, F. Xing, Use of nano-SiO_2 to develop a high performance green lightweight engineered cementitious composites containing fly ash cenospheres, J. Clean. Prod. 262 (2020) 121274. https://doi.org/10.1016/j.jclepro.2020.121274.

[26] J. Wang, X. Wang, S. Ding, A. Ashour, F. Yu, X. Lv, B. Han, Micro-nano scale pore structure and fractal dimension of ultra-high performance cementitious composites modified with nanofillers, Cem. Concr. Compos. 141 (2023) 105129. https://doi.org/10.1016/j.cemconcomp.2023.105129.

[27] Z. Wu, K.H. Khayat, C. Shi, B.F. Tutikian, Q. Chen, Mechanisms underlying the strength enhancement of UHPC modified with nano-SiO_2 and nano-$CaCO_3$, Cem. Concr. Compos. 119 (2021) 103992. https://doi.org/10.1016/j.cemconcomp.2021.103992.

[28] J. Jiang, X. Dong, H. Wang, F. Wang, Y. Li, Z. Lu, Enhanced mechanical and photocatalytic performance of cement mortar reinforced by nano-TiO_2 hydrosol-coated sand, Cem. Concr.

659 Compos. 137 (2023) 104906. https://doi.org/10.1016/j.cemconcomp.2022.104906.
660 [29] Y. Ding, J.P. Liu, Y.L. Bai, Linkage of multi-scale performances of nano-$CaCO_3$ modified
661 ultra-high performance engineered cementitious composites (UHP-ECC), Constr. Build.
662 Mater. 234 (2020) 117418. https://doi.org/10.1016/j.conbuildmat.2019.117418.
663 [30] M. Sun, J. Zhu, T. Sun, Y. Chen, X. Li, W. Yin, J. Han, Multiple effects of nano-$CaCO_3$ and
664 modified polyvinyl alcohol fiber on flexure-tension-resistant performance of engineered
665 cementitious composites, Constr. Build. Mater. 303 (2021) 124426.
666 https://doi.org/10.1016/j.conbuildmat.2021.124426.
667 [31] D. Pavan Kumar, S. Amit, M. Sri Rama Chand, Influence of various nano-size materials on
668 fresh and hardened state of fast setting high early strength concrete [FSHESC]: A state-of-
669 the-art review, Constr. Build. Mater. 277 (2021) 122299.
670 https://doi.org/10.1016/j.conbuildmat.2021.122299.
671 [32] A. Hosan, F.U.A. Shaikh, P. Sarker, F. Aslani, Nano- and micro-scale characterisation of
672 interfacial transition zone (ITZ) of high volume slag and slag-fly ash blended concretes
673 containing nano SiO_2 and nano $CaCO_3$, Constr. Build. Mater. 269 (2021) 121311.
674 https://doi.org/10.1016/j.conbuildmat.2020.121311.
675 [33] S. Kawashima, P. Hou, D.J. Corr, S.P. Shah, Modification of cement-based materials with
676 nanoparticles, Cem. Concr. Compos. 36 (2013) 8–15.
677 https://doi.org/10.1016/j.cemconcomp.2012.06.012.
678 [34] S. Yeşilmen, Y. Al-Najjar, M.H. Balav, M. Şahmaran, G. Yildirim, M. Lachemi, Nano-
679 modification to improve the ductility of cementitious composites, Cem. Concr. Res. 76
680 (2015) 170–179. https://doi.org/10.1016/j.cemconres.2015.05.026.
681 [35] S.A. Khokhar, T. Ahmed, R.A. Khushnood, M.U. Basit, Shahnawaz, S. Javed, Development
682 of low carbon engineered cementitious composite (ECC) using nano lime calcined clay
683 cement (nLC^3) based matrix, Case Stud. Constr. Mater. 20 (2024) e02669.
684 https://doi.org/10.1016/j.cscm.2023.e02669.
685 [36] ASTM C618-17a, Standard Specification for Coal Fly Ash and Raw or Calcined Natural
686 Pozzolan for Use in Concrete, ASTM International, West Conshohocken, PA, 2017.
687 [37] H. Zhu, D. Zhang, T. Wang, M. McBain, V.C. Li, Intrinsic self-stressing and low carbon

688 Engineered Cementitious Composites (ECC) for improved sustainability, Cem. Concr. Res.
689 149 (2021) 106580. https://doi.org/10.1016/j.cemconres.2021.106580.
690 [38] H. Li, L. Zhang, S. Ding, X. Shu, X. Wang, B. Han, Effects and mechanisms of incorporated
691 nanoparticles on the rheological performance of cement pastes, J. Build. Eng. 73 (2023)
692 106694. https://doi.org/10.1016/j.jobe.2023.106694.
693 [39] Q. Yuan, C. Shi, D. Jiao, Rheology of Fresh Cement-Based Materials: Fundamentals,
694 Measurements, and Applications, 2022. https://doi.org/10.1201/9781003265313.
695 [40] Z. Tang, C. Litina, A. Al-Tabbaa, Optimisation of rheological parameters and mechanical
696 properties of Engineered Cementitious Composites (ECC) using regression-based models,
697 Constr. Build. Mater. 310 (2021) 125281.
698 https://doi.org/10.1016/j.conbuildmat.2021.125281.
699 [41] G. Heirman, L. Vandewalle, D. Van Gemert, Ó. Wallevik, Integration approach of the
700 Couette inverse problem of powder type self-compacting concrete in a wide-gap concentric
701 cylinder rheometer, J. Nonnewton. Fluid Mech. 150 (2008) 93–103.
702 https://doi.org/10.1016/j.jnnfm.2007.10.003.
703 [42] A.R. Arunothayan, B. Nematollahi, K.H. Khayat, A. Ramesh, J.G. Sanjayan, Rheological
704 characterization of ultra-high performance concrete for 3D printing, Cem. Concr. Compos.
705 136 (2023) 104854. https://doi.org/10.1016/j.cemconcomp.2022.104854.
706 [43] ASTM C109/C109M-20b, Standard test method for compressive strength of hydraulic
707 cement mortars (Using 2-in. Or [50 mm] Cube Specimens), ASTM International, West
708 Conshohocken, PA, 2020.
709 [44] GB/T 50081, Chinese Code for Test Methods of Concrete Physical and Mechanical
710 Properties, Beijing, 2019.
711 [45] JSCE, Recommendations for Design and Construction of High Performance Fiber
712 Reinforced Cement Composites with Multiple Fine Cracks, Japan Soc. of Civil Engineers,
713 Tokyo, 2008.
714 [46] RILEM FMC-50, Determination of the fracture energy of mortar and concrete by means of
715 three-point bend tests on notched beams, 18 (1985) 287–290.
716 [47] H. Zhong, M.Z. Zhang, Effect of recycled tyre polymer fibre on engineering properties of

717 sustainable strain hardening geopolymer composites, Cem. Concr. Compos. 122 (2021)
718 104167. https://doi.org/10.1016/j.cemconcomp.2021.104167.
719 [48] M. Chen, L. Yang, Y. Zheng, Y. Huang, L. Li, P. Zhao, S. Wang, L. Lu, X. Cheng, Yield
720 stress and thixotropy control of 3D-printed calcium sulfoaluminate cement composites with
721 metakaolin related to structural build-up, Constr. Build. Mater. 252 (2020) 119090.
722 https://doi.org/10.1016/j.conbuildmat.2020.119090.
723 [49] C. Liu, X. Wang, Y. Chen, C. Zhang, L. Ma, Z. Deng, C. Chen, Y. Zhang, J. Pan, N. Banthia,
724 Influence of hydroxypropyl methylcellulose and silica fume on stability, rheological
725 properties, and printability of 3D printing foam concrete, Cem. Concr. Compos. 122 (2021)
726 104158. https://doi.org/10.1016/j.cemconcomp.2021.104158.
727 [50] K. Pasupathy, S. Ramakrishnan, J. Sanjayan, 3D concrete printing of eco-friendly
728 geopolymer containing brick waste, Cem. Concr. Compos. 138 (2023) 104943.
729 https://doi.org/10.1016/j.cemconcomp.2023.104943.
730 [51] D.Y. Yoo, T. Oh, N. Banthia, Nanomaterials in ultra-high-performance concrete (UHPC) – A
731 review, Cem. Concr. Compos. 134 (2022) 104730.
732 https://doi.org/10.1016/j.cemconcomp.2022.104730.
733 [52] K.H. Khayat, W. Meng, K. Vallurupalli, L. Teng, Rheological properties of ultra-high-
734 performance concrete — An overview, Cem. Concr. Res. 124 (2019) 105828.
735 https://doi.org/10.1016/j.cemconres.2019.105828.
736 [53] A. Yahia, K.H. Khayat, Analytical models for estimating yield stress of high-performance
737 pseudoplastic grout, Cem. Concr. Res. 31 (2001) 731–738. https://doi.org/10.1016/S0008-
738 8846(01)00476-8.
739 [54] Z. Xu, Z. Zhou, P. Du, X. Cheng, Effects of nano-limestone on hydration properties of
740 tricalcium silicate, J. Therm. Anal. Calorim. 129 (2017). https://doi.org/10.1007/s10973-017-
741 6123-9.
742 [55] J. Camiletti, A.M. Soliman, M.L. Nehdi, Effect of nano-calcium carbonate on early-age
743 properties of ultrahigh-performance concrete, Mag. Concr. Res. 65 (2013) 297–307.
744 https://doi.org/10.1680/macr.12.00015.
745 [56] M. Chen, Y. Wang, T. Zhang, M. Zhang, Behaviour of structural engineered cementitious

composites under dynamic tensile loading and elevated temperatures, Eng. Struct. 280 (2023) 115739. https://doi.org/10.1016/j.engstruct.2023.115739.

[57] Y. Wang, M. Chen, T. Zhang, M. Zhang, Hardening properties and microstructure of 3D printed engineered cementitious composites based on limestone calcined clay cement, Cem. Concr. Compos. 152 (2024) 105641. https://doi.org/10.1016/j.cemconcomp.2024.105641.

[58] K.Q. Yu, W.J. Zhu, Y. Ding, Z.D. Lu, J. tao Yu, J.Z. Xiao, Micro-structural and mechanical properties of ultra-high performance engineered cementitious composites (UHP-ECC) incorporation of recycled fine powder (RFP), Cem. Concr. Res. 124 (2019) 105813. https://doi.org/10.1016/j.cemconres.2019.105813.

[59] E.H. Yang, V.C. Li, Strain-hardening fiber cement optimization and component tailoring by means of a micromechanical model, Constr. Build. Mater. 24 (2010) 130–139. https://doi.org/10.1016/j.conbuildmat.2007.05.014.

[60] T. Kanda, V.C. Li, Practical design criteria for saturated pseudo strain hardening behavior in ECC, J. Adv. Concr. Technol. 4 (2006) 59–72. https://doi.org/10.3151/jact.4.59.

[61] K. De Weerdt, M.B. Ben Haha, G. Le Saout, K.O.O. Kjellsen, H. Justnes, B. Lothenbach, Hydration mechanisms of ternary Portland cements containing limestone powder and fly ash, Cem. Concr. Res. 41 (2011) 279–291. https://doi.org/10.1016/j.cemconres.2010.11.014.

[62] Q. Wang, J. Li, G. Yao, X. Zhu, S. Hu, J. Qiu, P. Chen, X. Lyu, Characterization of the mechanical properties and microcosmic mechanism of Portland cement prepared with soda residue, Constr. Build. Mater. 241 (2020). https://doi.org/10.1016/j.conbuildmat.2019.117994.

[63] Z. Wu, C. Shi, K.H. Khayat, S. Wan, Effects of different nanomaterials on hardening and performance of ultra-high strength concrete (UHSC), Cem. Concr. Compos. 70 (2016) 24–34. https://doi.org/10.1016/j.cemconcomp.2016.03.003.

[64] L.Y. Xu, B.T. Huang, V.C. Li, J.G. Dai, High-strength high-ductility Engineered/Strain-Hardening Cementitious Composites (ECC/SHCC) incorporating geopolymer fine aggregates, Cem. Concr. Compos. 125 (2022). https://doi.org/10.1016/j.cemconcomp.2021.104296.

[65] T. Zhang, H. Wang, M. Chen, L. Niu, W. Zhu, Effect of interfacial characteristics on

775 dynamic splitting behavior of quasi rock-concrete composite layer: Towards resilient tunnel
776 support against rock burst, Tunn. Undergr. Sp. Technol. 155 (2025) 106134.
777 https://doi.org/10.1016/j.tust.2024.106134.
778